Experimental study of the A(e,e 'pi(+)) [A (e, e prime pi superscript +)] reaction on H-1 [superscript 1 H], H-2 [superscript 2 H], C-12 [superscript 12 C], Al-27 [superscript 27 Al], Cu-63 [superscript 63 Cu], and Au-197 [superscript 197 Au]

Experimental study of the $A(e,e'\pi^+)$ reaction on ^{1}H, ^{2}H, ^{12}C, ^{27}Al, ^{63}Cu, and ^{197}Au

X. Qian,[1] T. Horn,[2,3] B. Clasie,[4] J. Arrington,[5] R. Asaturyan,[6] F. Benmokhtar,[2] W. Boeglin,[7] P. Bosted,[3] A. Bruell,[3] M. E. Christy,[8] E. Chudakov,[3] M. M. Dalton,[9] A. Daniel,[10] D. Day,[11] D. Dutta,[12,1] L. El Fassi,[5] R. Ent,[3] H. C. Fenker,[3] J. Ferrer,[13] N. Fomin,[11] H. Gao,[1] K. Garrow,[14] D. Gaskell,[3] C. Gray,[9] G. M. Huber,[15] M. K. Jones,[3] N. Kalantarians,[10] C. E. Keppel,[3,8] K. Kramer,[1] Y. Li,[10] Y. Liang,[16] A. F. Lung,[3] S. Malace,[8] P. Markowitz,[7] A. Matsumura,[17] D. G. Meekins,[3] T. Mertens,[18] T. Miyoshi,[10] H. Mkrtchyan,[6] R. Monson,[19] T. Navasardyan,[6] G. Niculescu,[13] I. Niculescu,[13] Y. Okayasu,[17] A. K. Opper,[16] C. Perdrisat,[20] V. Punjabi,[21] A. W. Rauf,[22] V. M. Rodriquez,[10] D. Rohe,[18] J. Seely,[4] E. Segbefia,[8] G. R. Smith,[3] M. Sumihama,[17] V. Tadevosyan,[6] L. Tang,[3,8] A. Villano,[23] W. F. Vulcan,[3] F. R. Wesselmann,[21] S. A. Wood,[3] L. Yuan,[8] and X. Zheng[5]

[1]*Triangle Universities Nuclear Laboratory, Duke University, Durham, North Carolina, USA*
[2]*University of Maryland, College Park, Maryland, USA*
[3]*Physics Division, TJNAF, Newport News, Virginia, USA*
[4]*Laboratory for Nuclear Science, Massachusetts Institute of Technology, Cambridge, Massachusetts, USA*
[5]*Argonne National Laboratory, Argonne, Illinois, USA*
[6]*Yerevan Physics Institute, Yerevan, Armenia*
[7]*Florida International University, Miami, Florida, USA*
[8]*Hampton University, Hampton, Virginia, USA*
[9]*University of the Witwatersrand, Johannesburg, South Africa*
[10]*University of Houston, Houston, Texas, USA*
[11]*University of Virginia, Charlottesville, Virginia, USA*
[12]*Mississippi State University, Mississippi State, Mississippi, USA*
[13]*James Madison University, Harrisonburg, Virginia, USA*
[14]*TRIUMF, Vancouver, British Columbia, Canada*
[15]*University of Regina, Regina, Saskatchewan, Canada*
[16]*Ohio University, Athens, Ohio, USA*
[17]*Tohoku University, Sendai, Japan*
[18]*Basel University, Basel, Switzerland*
[19]*Central Michigan University, Mount Pleasant, Michigan, USA*
[20]*College of William and Mary, Williamsburg, Virginia, USA*
[21]*Norfolk State University, Norfolk, Virginia, USA*
[22]*University of Manitoba, Winnipeg, Manitoba, Canada*
[23]*Rensselear Polytechnic Institute, Troy, New York, USA*

(Received 12 August 2009; revised manuscript received 6 April 2010; published 25 May 2010)

Cross sections for the ^{1}H$(e,e'\pi^+)n$ process on ^{1}H, ^{2}H, ^{12}C, ^{27}Al, ^{63}Cu, and ^{197}Au targets were measured at the Thomas Jefferson National Accelerator Facility (Jefferson Lab) to extract nuclear transparencies. Data were taken from $Q^2 = 1.1$–4.7 GeV^2 for a fixed center-of-mass energy of $W = 2.14$ GeV. The ratio of σ_L and σ_T was extracted from the measured cross sections for ^{1}H, ^{2}H, ^{12}C, and ^{63}Cu targets at $Q^2 = 2.15$ and 4.0 GeV^2, allowing for additional studies of the reaction mechanism. In this article, we present the experimental setup and the analysis of the data in detail, including systematic uncertainty studies. Differential cross sections and nuclear transparencies as a function of the pion momentum at different values of Q^2 are presented. Our results are consistent with the predicted early onset of color transparency in mesons. Global features of the data are discussed and the data are compared with model calculations for the ^{1}H$(e,e'\pi^+)$n reaction from nuclear targets.

DOI: 10.1103/PhysRevC.81.055209 PACS number(s): 14.40.Be, 11.55.Jy, 13.40.Gp, 13.60.Le

I. INTRODUCTION

A fundamental challenge in nuclear physics is to understand the structure of hadrons in terms of their quark-gluon constituents, which are governed by the underlying theory of the strong interaction, quantum chromodynamics (QCD). Measurements of exclusive processes, such as pion electroproduction, make it possible to extract meson form factors and study quark-gluon distributions in the nucleon. However, to develop a description of atomic nuclei based on QCD, one also needs to understand how the properties and interactions of hadrons change in the nuclear medium. Measurements of exclusive processes in the nuclear medium are helpful in this regard, because QCD has definite predictions for exclusive processes in the medium. One such prediction is the phenomenon of color transparency (CT).

CT was first proposed by Brodsky and Mueller [1] in 1982 and refers to the vanishing of the hadron-nucleon interaction for hadrons produced in exclusive processes inside a nucleus. At sufficiently high momentum transfers, the hadron is produced with small transverse size, $b_\perp \approx 1/Q$ [2]. The fast-moving hadron also has a compact longitudinal size owing to Lorentz contraction. Such a reduced-size quark-gluon state is called a pointlike configuration (PLC). In the study of CT,

one investigates the interplay between the creation of quark systems with small transverse size, as predicted by QCD, and the possible suppression of interactions of such PLC with the nuclear medium. The onset of CT is expected at lower energies for the production of mesons than for the production of baryons because the quark-antiquark pair is more likely to form a small-size object [3]. Thus, pion electroproduction is a natural choice for an initial CT study.

As a further motivation, it is worthwhile to note that CT has recently been put into the context of a QCD factorization theorem [4] for longitudinally polarized photons in meson electroproduction. It predicts that for sufficiently high values of Q^2, at fixed $x = Q^2/(2M\nu)$ and fixed momentum transfer to the nucleon, $-t$, the amplitude can be expressed in terms of a short-distance (hard) process, a distribution amplitude describing the final-state meson, and generalized parton distributions (GPDs) [5]. The latter describe the long-distance (soft) physics. The factorization theorem has been proven at asymptotically high Q^2, but showing its validity at finite, high Q^2 requires stringent tests of all necessary conditions. The unambiguous observation of the onset of CT is a critical precondition for the validity of the factorization theorem [6]. This is because where CT applies, the outgoing meson retains a small transverse size (interquark distance) while soft interactions like multiple gluon exchange between the meson produced from the hard interaction and the baryon are highly suppressed. QCD factorization is thus rigorously not possible without CT.

A complication to the CT phenomenon is introduced by the formation time of the final-state hadron, which limits the lifetime of the PLC. The formation time refers to the time elapsed from the initial quark-photon interaction to the formation of the final-state hadron. In general, the formation of a PLC requires the high-momentum transfer scattering to select amplitudes in the initial- and final-state hadrons characterized by a small transverse size. In addition, the PLC should be "color neutral" outside of its small radius so as not to radiate gluons. Furthermore, the PLC should be maintained for some distance in traversing the nuclear medium. To understand the CT phenomenon, it is thus important to study the dependencies of the relevant experimental observables upon the four-momentum transfer squared of the virtual photon, Q^2 (the size of the initial PLC typically scales as $\sim 1/Q$), the hadron momentum (formation length), and the target mass A (path length through the medium).

Nuclear transparency is a natural observable in the quest to identify the onset of CT. Nuclear transparency is defined as the ratio of the cross section per nucleon for a process on a bound nucleon inside a nucleus to that on a free nucleon. Because the nuclear medium is not opaque to hadrons, CT will lead to an increase in nuclear transparency as a function of momentum transfer and hadron momentum. In addition, the A dependence of the nuclear transparency will show a Q^2 dependence. This simultaneous change of nuclear transparency with A and Q^2 is distinct from other conventional processes, such as rescattering. Moreover, it illustrates the need for a careful design of the experiment to simultaneously measure the Q^2 and A dependence of nuclear transparency and at the same time test alternative reaction mechanisms that can give rise to potential increases in nuclear transparency that mimic CT.

With the availability of high-intensity, continuous electron beams up to 6 GeV at Jefferson Lab, it has become possible for the first time to determine simultaneously the A and Q^2 dependence of the differential pion cross section for $Q^2 = 1$–5 GeV^2. These data were taken in 2004 with ^{1}H, ^{2}H, ^{12}C, ^{27}Al, ^{63}Cu, and ^{197}Au targets. The A and Q^2 dependence of the extracted nuclear transparencies were published in Ref. [7]. The purpose of this work is to discuss the experiment and analysis in detail and present and discuss additional results. This article is organized as follows: Sections II and III present methods for extracting nuclear transparencies and the findings of earlier studies. Section IV introduces the basic cross-section formalism of pion electroproduction. Sections V and VI describe the experimental setup and the data analysis. The determination of the cross sections and the extraction of the nuclear transparencies and their associated uncertainties are described in Secs. VII and VIII. The results, including the global features of the cross-section ratios and nuclear transparencies, and a comparison with results of recent calculations are presented in Sec. IX.

II. METHODS OF DETERMINING NUCLEAR TRANSPARENCY FROM DATA

In a simple picture of pion electroproduction on a nucleus, the electron exchanges a virtual photon with a proton that is moving because of its Fermi momentum. The struck proton ejects a positively charged pion (quasifree approximation) and turns into a neutron. The ejected pion may interact with the residual nucleons and the fraction of pions which can escape from the nucleus is the pion nuclear transparency. In reality, the scattering process is more complicated and deviations from this picture reveal much about the nucleus and its constituents. In the quasifree picture, the ratio of the longitudinal to the transverse cross section from a bound proton inside the nucleus is expected to be the same as that from a free proton. The plausibility of the quasifree approximation can thus be addressed by comparing the ratios of the longitudinal to the transverse cross sections from nuclear targets with those obtained from a nucleon target. Differences in the behavior of these ratios would indicate the effect of the nuclear medium, resulting in the breakdown of the quasifree assumption.

Assuming the dominance of the quasifree process, one can extract the nuclear transparency of the pions by taking the ratio of the acceptance-corrected cross sections from the nuclear target to those from the proton. In practice, these acceptance-corrected cross sections are equivalent to the ratio of yields from data ($\bar{Y}_{\rm data}$) to Monte Carlo (MC) ($\bar{Y}_{\rm MC}$). Therefore, the nuclear transparency is defined as:

$$T = (\bar{Y}_{\rm data}/\bar{Y}_{\rm MC})_A/(\bar{Y}_{\rm data}/\bar{Y}_{\rm MC})_H, \quad (1)$$

where A refers to a target with nuclear target and H is hydrogen. Nuclear transparency quantifies the interactions of the outgoing pion with the residual nucleons and is thus the key observable in searching for CT effects.

The formation length, the distance over which the PLC travels before the hadron reaches its final size, can be written as

$$l_f \approx \frac{\beta T_{\rm lifetime}}{\sqrt{1-\beta^2}}, \quad (2)$$

assuming a linear expansion in time, where β is the speed of the hadron in the laboratory frame and T_{lifetime} is the lifetime of the PLC in its rest frame. QCD predicts that the cross section for the interaction of a small $q\bar{q}$ dipole is proportional to b^2 in the leading-order approximation, where b is the transverse separation between the q and the $\bar{q}$. If the $q\bar{q}$ dipole remains small (pointlike) over the range of the nuclear system, the nucleus will be transparent to the produced hadron. This can be accomplished at large momentum transfers, where the formation length is sufficiently large.

At finite energies, however, the mechanism for the expansion and contraction of the interacting small system is more complex. The quantum diffusion model [8] assumes that quarks separate in the transverse direction at the speed of light and that their quark separation is proportional to $\sqrt{z}$, where z is the longitudinal distance from the production point to the position of the particle. The formation length in this model is determined from the average value of the dominant energy denominator,

$$l_f \approx 2P_h \left\langle \frac{1}{M_n^2 - M_h^2} \right\rangle, \tag{3}$$

where P_h and M_h are the momentum and mass of the hadron, respectively, while M_n is the mass of a typical intermediate state of the hadron. The precise value for $\Delta M^2 = (M_n^2 - M_h^2)$ is a matter of great uncertainty [8,9], with estimates ranging between 0.25 and 1.4 GeV^2.

Coherence length is defined as the distance over which the virtual photon fluctuates into a $q\bar{q}$ pair and for large coherence length, the virtual $q\bar{q}$ pair may undergo interactions with the nucleus before the hard interaction that puts it on shell. A coherence length dependence of the transparency, where the nuclear transparency decreases with an increase of the coherent length, can mimic a CT-like energy dependence. In pion electroproduction, the coherence length is given by $l_c = \frac{1}{2xM_n} = \frac{\nu}{Q^2}$, where $x = Q^2/(2M_n\nu)$ is the Bjorken scaling variable x and $\nu = E - E'$ is the energy loss of the incident electron. The coherence length of the pion in this experiment ranges from 0.2 to 0.5 fm, which makes it essentially constant and very small. This removes any coherence length dependence of the transparency through t-channel π-ρ exchange.

III. EARLY EXTRACTIONS OF NUCLEAR TRANSPARENCY

The first experiments designed to search for CT used the $^{12}C(p,2p)$ reaction with a fixed target and were performed at Brookhaven National Laboratory [10–12]. The nuclear transparency initially increased as a function of the beam energy and then decreased, with a peak near 9 GeV. Though this behavior was not predicted by traditional nuclear physics calculations, it is currently not attributed to CT. Instead, it is believed to be associated with nuclear filtering [13,14], which is related to the suppression of the long-range components in the wave function, or to the threshold for charm resonance production [15].

The nuclear transparency was also measured using the $A(e,e'p)$ reaction at the Stanford Linear Accelerator Center [16,17] and at Jefferson Lab [18,19]. The nuclear transparency was found to be energy independent from $Q^2 \approx 2$–8.1 GeV^2 for deuterium, carbon, iron, and gold targets, thus indicating no significant CT effect. The absence of the CT effect in this channel has been interpreted as an indication that the proton formation length may only have been as large as internucleonic distances, rather than the size of the nucleus in these experiments [20].

CT measurements using coherent and incoherent ρ^0 production have been performed at Fermilab [21] and more recently at DESY [22]. The nuclear transparency results from Fermilab were parametrized with a function $T = A^{\alpha-1}$, and at a first glance, the observed positive slope of α as a function of Q^2 appeared to contradict the flat Q^2 dependence predicted by the Glauber multiple-scattering mechanism [23]. However, the results have since been interpreted as a coherence length effect [24], in which for kinematics with large coherence length, the virtual $q\bar{q}$ pair may undergo interactions with the nucleus before the hard interaction that puts it on shell. The kinematics of the Fermilab experiment were not at a constant l_c, and thus the variation of α with Q^2 was attributed to a reduction in initial state interactions rather than to a reduction in final-state interactions. The more recent measurements from DESY, ranging between $Q^2 = 0.9$ GeV^2 and $Q^2 = 3$ GeV^2 and at constant l_c, showed a rise in nuclear transparency, with Q^2 consistent with theoretical calculations of CT [22].

The most convincing evidence for the existence of CT comes from an experiment performed at Fermilab [25]. There, the cross section of diffractive dissociation of 500 GeV/c pions into dijets was measured and parametrized with $\sigma = \sigma_0 A^\alpha$, where σ_0 is the π-N cross section in free space. The free parameter, α, was fit to the data with the result $\alpha \sim 1.6$. This result was in agreement with calculations assuming 100% CT and was very different from the normal π-N cross section, which has a dependence $\sigma = \sigma_0 A^{2/3}$.

At low energies, hints of CT effects have also been observed via pion photoproduction from helium, $^4\text{He}(\gamma,\pi^- p)$, at Jefferson Lab [26]. CT can be measured in these reactions, where $Q^2 = 0$, by measuring the cross section versus the four-momentum transfer squared, t, to the hadron system. The data showed 2σ deviations from the traditional Glauber calculations and the slope of the data vs $-t$ was in better agreement with calculations including CT.

IV. ELEMENTARY PION ELECTROPRODUCTION

A. Kinematics

The kinematic variables of the pion electroproduction reaction are shown in Fig. 1. The incident electron has a three-momentum of $\mathbf{k}$. The scattered electron has a three-momentum $\mathbf{k}'$ and travels at a polar angle θ_e in the laboratory frame with respect to the direction of the incident beam. The three-momentum vectors of the incoming and outgoing electron define the scattering plane. The corresponding four-momenta are $k \equiv (E, \mathbf{k})$ and $k' \equiv (E', \mathbf{k}')$. The virtual photon carries a four-momentum $q \equiv (\omega, \mathbf{q})$, which is given by $q \equiv k - k'$.

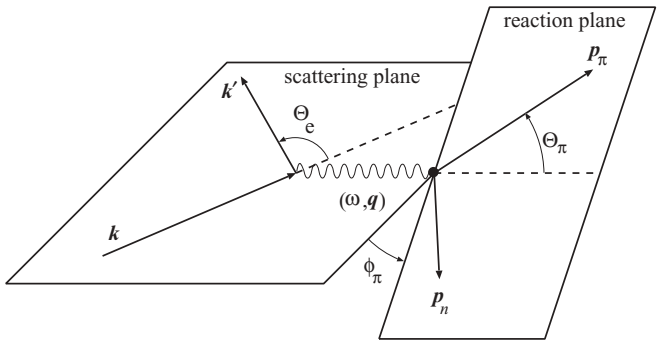

FIG. 1. Kinematic variables of the ^{1}H$(e,e',\pi^+)n$ reaction in the laboratory frame.

The reaction plane is defined by the three-momentum **q** and the three-momentum vector of the produced pion $\mathbf{P}_\pi$ and makes an angle ϕ_π with respect to the scattering plane. The angle (in the laboratory system) between $\mathbf{p}_\pi$ and **q** is θ_π.

The pion electroproduction reaction can be described using three Lorentz invariants. In addition to Q^2, we use the invariant mass of the virtual photon-nucleon system, W, which can be expressed as $W = \sqrt{M_p^2 + 2M_p\omega - Q^2}$, where M_p is the proton mass and $t = (P_\pi - q)^2$ is the Mandelstam variable.

B. Cross sections

The pion electroproduction cross section from a stationary proton in the one-photon-exchange approximation is [27]

$$\frac{d^5\sigma}{d\Omega_{e'}dE_{e'}d\Omega_\pi} = \Gamma_\nu \frac{d^2\sigma}{d\Omega_\pi}, \tag{4}$$

where

$$\Gamma_\nu = \frac{\alpha}{2\pi^2}\frac{E_{e'}}{E_e}\frac{K_{\rm eq}}{Q^2}\frac{1}{1-\epsilon} \tag{5}$$

is the virtual photon flux, and α is the fine structure constant. The factor $K_{\rm eq} = (W^2 - M_p^2)/(2M_p)$ is the equivalent photon energy, and

$$\epsilon = \left(1 + \frac{2|\mathbf{q}|^2}{Q^2}\tan^2\frac{\theta_e}{2}\right)^{-1} \tag{6}$$

is the longitudinal polarization of the virtual photon. The twofold differential cross section for a stationary proton target can be written as

$$\frac{d^2\sigma}{d\Omega_\pi} = J\frac{d^2\sigma}{dtd\phi}, \tag{7}$$

where the solid angle of the pion, Ω_π, is determined in the laboratory frame, and J is the Jacobian for the transformation from Ω_π to t,ϕ. The twofold cross section can be separated into four structure functions, which correspond to the polarization states of the virtual photon, a longitudinal (L), a transverse (T), and two interference terms (LT and TT):

$$2\pi\frac{d^2\sigma}{dtd\phi} = \epsilon\frac{d\sigma_{\rm L}}{dt} + \frac{d\sigma_{\rm T}}{dt} + \sqrt{2\epsilon(\epsilon+1)}\frac{d\sigma_{\rm LT}}{dt}\cos\phi + \epsilon\frac{d\sigma_{\rm TT}}{dt}\cos 2\phi. \tag{8}$$

The interference terms vanish in parallel kinematics ($\theta_\pi = 0$) because of their dependence on θ_π [28].

The four structure functions can be separated if measurements at different values of ϵ and ϕ are performed (L/T separation), with W, Q^2, and t kept constant. The photon polarization ϵ can be varied by changing the electron energy and the scattering angle. For nuclei, where there is a new degree of freedom owing to the Fermi momentum of the struck nucleon, the differential pion electroproduction cross section is given by

$$\frac{d^6\sigma}{d\Omega_{e'}dE_{e'}d\Omega_\pi dP_\pi} = \Gamma_\nu\frac{d^3\sigma}{d\Omega_\pi dP_\pi}. \tag{9}$$

The threefold differential cross section, $\frac{d^3\sigma}{d\Omega_\pi dP_\pi}$, can be separated into longitudinal, transverse, and interference terms just as in Eqs. (7) and (8).

V. EXPERIMENT AND SETUP

The E01-107 experiment (pionCT) was carried out in Hall C at Jefferson Lab [29] in 2004. A schematic view of the experimental setup is shown in Fig. 2 and the kinematic settings of the measurements are listed in Table I. The continuous-wave (100% duty factor) electron beam from the CEBAF accelerator has a characteristic 2-ns microstructure that arises from the 1.5-GHz rf structure of the accelerator and the three-hall beam-splitting scheme. This 2-ns structure is used in the data analysis to identify $(e,e'\pi^+)$ coincident events. The electron beam, with energies of up to 5.8 GeV, was incident on liquid hydrogen and deuterium cryotargets and solid foil targets of ^{12}C, ^{27}Al, ^{63}Cu, and ^{197}Au. For the cryotargets, a 4.0-cm-diameter cylindrical cell with axis perpendicular to the beam direction was used. The cell walls were made from an aluminum alloy with a thickness of 0.01 cm. The beam current (35–80 μA) was measured using a pair of microwave cavities with a DC current transformer to an accuracy of 0.4%. To reduce target density fluctuations in the cryotargets arising from beam heating, the beam was rastered to a 2×2-mm^2 profile. The position of the beam was recorded in the data stream for each event. The reconstruction can therefore be corrected for the vertical position of the beam, event by event. The target density fluctuations were measured to an accuracy of 0.6%.

The scattered electrons were detected in the short-orbit spectrometer (SOS). The SOS consists of three non-superconducting magnets, one quadrupole followed by two dipoles, which share a common yoke. The quadrupole focuses in the nondispersive direction, the first dipole bends particles with the central momentum upward by 33°, and the second one bends them downward by 15°. The SOS spectrometer design was optimized for the detection of unstable and short-lived particles and thus has a flight path of only 10 m. The electroproduced pions were detected in the high-momentum spectrometer (HMS). The HMS consists of three superconducting quadrupole magnets, followed by a momentum analyzing vertical-bend superconducting dipole used in a point-to-point tune for the central ray. The detector package is mounted near the focal plane of the optical system,

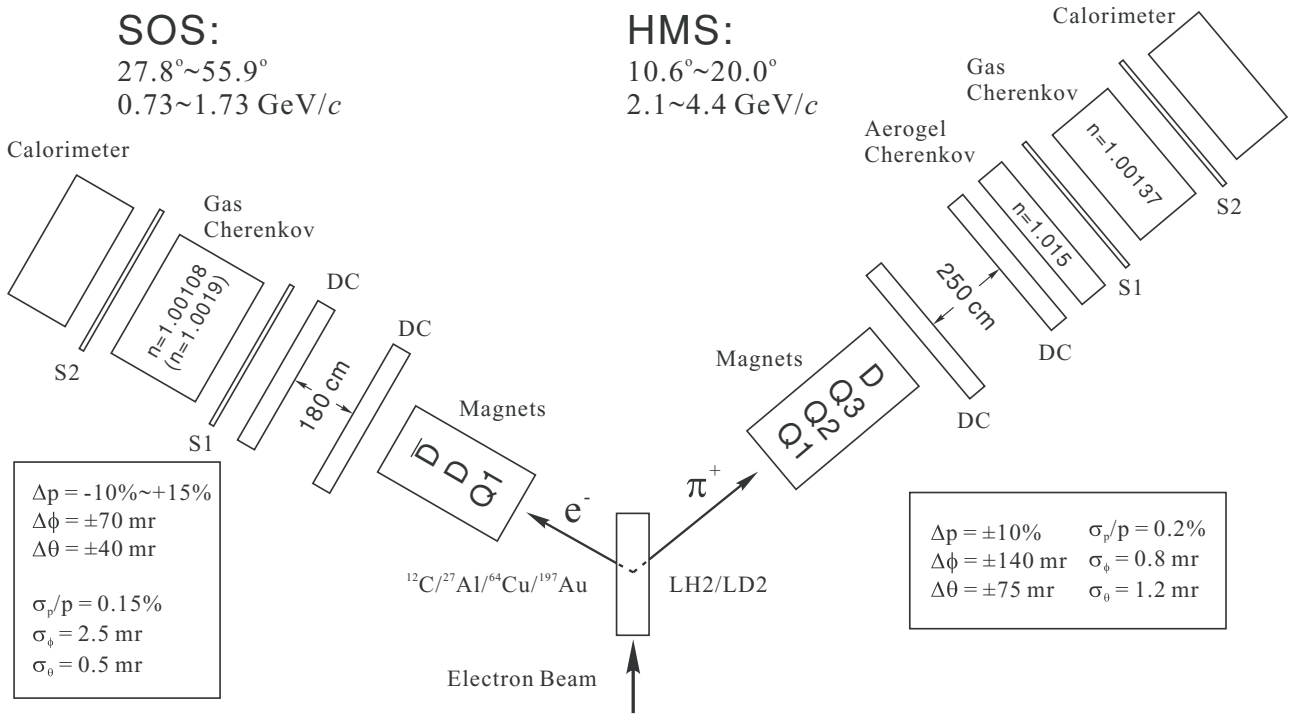

FIG. 2. Schematic view of the experimental setup for E01-107.

which is located inside a concrete shield house. The HMS has a 26-m pathlength and a maximum central momentum of 7.3 GeV. A detailed description of the spectrometers and the spectrometer hardware is given in Refs. [30,31]. Selected properties of the two spectrometers are listed in Table II.

Both spectrometers are equipped with multiwire drift chambers for particle tracking and segmented scintillator hodoscope arrays for time-of-flight measurements and triggering.

The HMS has a gas Čerenkov and a lead-glass calorimeter in the detector stack for K^+/π^+ separation. For this experiment, the Čerenkov was filled with C_4F_{10} gas at 97 kPa. The corresponding index of refraction is 1.00137, resulting in momentum thresholds of 2.65 GeV/c for π^+ and 9.4 GeV for K^+. An aerogel Čerenkov detector [32] was also used in the detector stack. It was used to identify π^+ for central momentum settings below 3.1 GeV/c. The aerogel had an index of refraction of 1.015, giving thresholds of 0.8 GeV/c for pions and 2.85 GeV/c for kaons.

The SOS is instrumented with a combination of a gas Čerenkov and a lead-glass calorimeter for e^-/π^- separation. The nominal SOS Čerenkov detector is filled with CCl_2F_2 gas at 101 kPa, with an index of refraction of 1.00108. During part of the experiment ($E_e = 5.767$ GeV), the nominal SOS Čerenkov detector was replaced with a new one filled with C_4F_{10} gas at 143 kPa with an index of refraction of 1.0019. The

TABLE I. The central kinematic settings for the pion transparency experiment. θ_q is the angle between the virtual photon three-momentum **q** and the beam direction in the laboratory frame and k_π is the magnitude of the three-momentum of the virtual struck pion in the quasifree knockout picture ($\mathbf{k}_\pi = \mathbf{p}_\pi - \mathbf{q}$).

Q^2 (GeV^2)	W (GeV)	$-t_{\min}$ (GeV^2)	E (GeV)	θ_e (deg)	E' (GeV)	θ_π (deg)	P_π (GeV/c)	k_π (GeV/c)	ϵ
1.10	2.26	0.050	4.021	27.76	1.190	10.61	2.793	0.23	0.50
2.15	2.21	0.158	5.012	28.85	1.730	13.44	3.187	0.41	0.56
3.00	2.14	0.289	5.012	37.77	1.430	12.74	3.418	0.56	0.45
3.91	2.26	0.413	5.767	40.38	1.423	11.53	4.077	0.70	0.39
4.69	2.25	0.527	5.767	52.67	1.034	10.63	4.412	0.79	0.26
2.16[a]	2.21	0.164	4.021	50.76	0.730	10.60	3.187	0.42	0.27
4.01[b]	2.14	0.441	5.012	55.88	0.910	10.55	3.857	0.71	0.25
2.16[c]	1.74	0.374	4.021	32.32	1.730	19.99	2.074	0.65	0.63

[a]Low ϵ setting used for L-T separations.
[b]Low ϵ setting used for L-T separations.
[c]Test point for checking the dependence on W and k_π.

TABLE II. Selected properties for the HMS and SOS spectrometers.

Quantity	HMS	SOS
Max. central mom. (GeV/c)	7.3[a]	1.74
Optical length (m)	26.0	7.4
Momentum acceptance (%)	±10	±20
Solid angle (msr)[b]	6.7	7.5
In-plane ang. acc. (mrad)[a]	±27.5	±57.5
Out-of-plane ang. acc. (mrad)[a]	±70	±37.5

[a]To date, the HMS has been operated to 6.0 GeV/c.
[b]The solid angle and angular acceptances are given for the large collimators in both the HMS and SOS spectrometers.

corresponding thresholds for electrons were below 10 MeV/c, and those for pions were 3 GeV/c (nominal) or 2.27 GeV/c ($E_e = 5.767$ GeV).

VI. DATA ANALYSIS

The raw data were processed and combined with additional information from the experiment, such as the central momentum and angle settings of the spectrometers, the detector positions and beam energy to give particle trajectories and momenta, and energy deposition to perform particle identification.

A. Event reconstruction

The spectrometer quantities x, y, x', and y' were deduced from reconstruction of the wire chamber data. These quantities are the vertical and horizontal positions of a track at the midpoint between the wire chambers, and the gradients of that track with respect to the spectrometer central ray. The target quantities $y_{\rm tar}$, $x'_{\rm tar}$, $y'_{\rm tar}$, and δ were determined from the spectrometer quantities by suitable transformation functions. These quantities are the horizontal position of the event, the horizontal and vertical gradients of the track with respect to the spectrometer central ray, and the momentum of the particle given as a percentage above the central momentum setting of the spectrometer, respectively. A special data set, using a series of foil targets placed at well determined positions in the target region, was taken to calibrate the transformation matrix.

B. Particle identification and event selection

Electrons were selected with a SOS gas Čerenkov cut of number of photoelectrons, $N_{\rm ph} > 1.0$ for the nominal detector, or $N_{\rm ph} > 5.0$ for the new detector. The efficiency of the cut was determined, for each of the SOS central momentum settings, using a sample of electrons that was identified using the lead-glass calorimeter. The resulting efficiency was always higher than 99.2%, with an uncertainty of 0.2%. The pion rejection ratio was 100 : 1 for the nominal detector and 300 : 1 for the new detector during the $E_e = 5.767$ GeV run. In the HMS, the aerogel and gas Čerenkov detectors were used to select π^+. The aerogel was used for additional particle identification when the central momentum setting of the HMS, $P_{\rm HMS}$, was less than 3.2 GeV/c. The lower limit of the aerogel efficiency was determined using tight cuts on the coincidence time and was found to be $>98.8 \pm 0.5\%$ for a threshold cut of $N_{\rm ph} > 0.7$. The rejection ratio for the HMS aerogel Čerenkov detector was approximately 5 : 1 at $P_{\rm HMS} =$ 2.1 and 2.8 GeV/c. A cut on the gas Čerenkov detector, varying between $N_{\rm ph} >0.7$ and $N_{\rm ph} >2.0$, was used when $P_{\rm HMS} \geqslant 3.2$ GeV/c. The corresponding cut efficiencies were determined using tight cuts on the coincidence time and the aerogel Čerenkov detector to remove protons and were found to be $>98.2 \pm 0.5\%$. The cut efficiency was parametrized as a function of the HMS fractional momentum, $\delta_{\rm HMS}$, to take into account the fact that pions at negative $\delta_{\rm HMS}$ are closer to the momentum threshold of the detector than those at positive $\delta_{\rm HMS}$. The resulting rejection ratio was 50 : 1 at $P_{\rm HMS}$=3.2 GeV/c and 300 : 1 at $P_{\rm HMS} = 4.4$ GeV/c with an uncertainty of 0.2%.

C. Efficiencies

The raw yield was normalized by the beam charge, and the data were corrected for detector efficiencies, computer dead time, correction to target thickness, and nuclear absorption in the detection materials.

1. Tracking efficiency

The tracking efficiency is the probability of finding a track from experimental signals from the wire chambers when a charged particle passes through them. It depends on the intrinsic efficiency of the wire chambers and on the algorithm used to construct a track for a given event. The tracking efficiency was >92% for the HMS and >96% for the SOS and was calculated on a run-by-run basis for this experiment. The uncertainties in the tracking efficiencies were estimated from the stability of the tracking efficiencies as a function of the total rate in the spectrometer and were found to be 1.0% for the HMS and 0.5% for the SOS. The rate dependence of the tracking efficiency is related to the increased probability of multiple tracks at higher rates. The tracking efficiency calculation corrects for an observed bias in the reconstruction algorithm, owing to the exclusion of two track events, using the method outlined in Ref. [33].

2. Trigger efficiency

The HMS and the SOS spectrometers each contain four layers of scintillators. The single-arm trigger for each spectrometer was that three out of four layers must have a hit. The three-out-of-four efficiency was found to be above 99.5% for all runs, with an uncertainty of 0.5% for both spectrometers.

3. Computer and electronics dead times

The computer dead time, which is attributable to the finite time required by the computers to process an event, can be directly calculated from the number of generated pretriggers and the number of accepted triggers. The computer dead time during the pionCT experiment was about 25%. The electronics dead time, owing to the finite time required by

the electronic modules, was estimated from copies of the original pretrigger signal at varying gate widths. The correction owing to the electronics dead time was less than 1%. The total uncertainty (0.2%–0.5%) owing to the dead time corrections was dominated by the computer dead time.

4. Coincidence blocking

Coincidence events can be blocked when a noncoincident event arrives in one of the spectrometers just before the coincident event. The "coincidence-blocking" events are lost from the data owing to the coincidence time cuts in the analysis. The coincidence blocking correction was estimated from the rate dependence of the number of blocked events and was found to be less than 0.7%, with an uncertainty of about 0.2%.

5. Pion absorption

Pions may interact through the strong nuclear force with nuclei, for instance in the target material, in the window of the scattering chamber, or the windows of the spectrometer. These events are lost before reaching the detectors in the HMS detector hut. We account for these events by correcting for pion absorption in the HMS detectors. The transmission for pions in the HMS is about 95% [34] and depends weakly on the pion momentum between 2.1 and 4.4 GeV/c. In addition, some pions interact with the scintillator material, producing events that reconstruct with too-low pion velocity (β_π) or even $\beta_\pi = 0$ and lower coincidence time. Using a two-dimensional cut on β_π and coincidence time, such events were included in our pion yield. The efficiency of such a cut was studied using $(e,e'\pi^-)$ [33] and H$(e,e'p)$ [33,35] data. The difference between the two-dimensional cut and a simple cut on pion velocity was found to be within the uncertainty associated with the HMS detector efficiency and the uncertainty of the pion absorption correction. The uncertainty in the pion absorption correction was estimated from the difference between the calculated pion transmission and the measured pion transmission and was found to be 2% in the absolute cross-section determination [34,36]. The difference in target thickness leads to an additional A-dependent uncertainty, which is estimated to be 0.5%.

6. Backgrounds

The coincidence time was calculated from the time difference between the SOS and the HMS triggers and was used to help identify e^-/π^+ coincidences from e^-/p coincidences. Corrections to the coincidence time include the path lengths of the tracks through the magnetic elements of the spectrometer, differences in signal propagation times in cables, pulse height corrections for the signals from the scintillators, and subtraction of the time required for the light to travel in the scintillators from the event position to the PMT. Random coincidences, resulting from an electron and pion from different beam buckets, have a coincidence time that is offset from the in-time events by multiples of 2 ns. The in-time e^-/π^+ events were selected with a cut on the coincidence time around the central peak. The random background was estimated by averaging over three bunches to the right and three bunches to the left of the in-time peak and subtracted from the in-time yield.

Background from the cryotarget cell walls, less than a few percent, was measured and subtracted using an aluminum target of approximately seven times the thickness of the target cell walls. (The aluminum target was seven times thicker to equalize the multiple scattering contributions.) The contribution of the cell walls was small (less than 5%) and, owing to the high statistical accuracy of the dummy target data, the contribution of the subtraction to the total uncertainty was $<0.1\%$.

7. Missing mass

Once true e^-/π^+ coincidences are identified, the missing mass of the recoiling nucleon system was reconstructed from the measured quantities. In the analysis presented here, a cut on the missing mass was used to ensure that no additional pions were produced in the case of hydrogen and to minimize the contribution of multipion events from nuclei to less than 5% with an uncertainty of $<0.4\%$ (see Sec. VII A4 for a more detailed discussion).

VII. DETERMINATION OF THE CROSS SECTION AND THE NUCLEAR TRANSPARENCY

To extract cross section information from the data, the measured yields were compared to the results of a Monte Carlo simulation for the actual experimental setup (see Sec. VII A), which included a realistic model of the pion electroproduction cross section. If the model can accurately describe the W, Q^2, t, and θ_π (P_π) dependence of the four structure functions in Eq. (8), the bin-centered cross section for any value of W and Q^2 in the acceptance can be determined as

$$\left(\frac{d\sigma}{dt}\right)_{\text{data}} = \frac{Y_{\text{data}}}{Y_{\text{MC}}}\left(\frac{d\sigma}{dt}\right)_{\text{MC}}, \tag{10}$$

where Y is the yield over W and Q^2 and the terms with "data" refer to the measured experimental yields, and the terms with "MC" refer to the simulated yields. The Monte-Carlo point cross section is calculated at the bin center; therefore, Eq. (10) also describes the bin-centering procedure.

The nuclear transparency is defined as the ratio of cross sections extracted from data and from a model of pion electroproduction from the nucleus without π-N final-state interactions. To extract the nuclear transparency, simulations were performed to obtain the cross-section ratio from model (Sec. VII A). Because the data for the hydrogen and nuclear targets were taken under exactly the same experimental conditions, bin centering was not required in the formation of the ratio. Instead, the ratios of yields (or the ratios of average cross sections) were used. The average cross sections were also used in the extraction of the ratio of longitudinal to transverse cross sections in Sec. VII A5 to test the quasifree reaction mechanism.

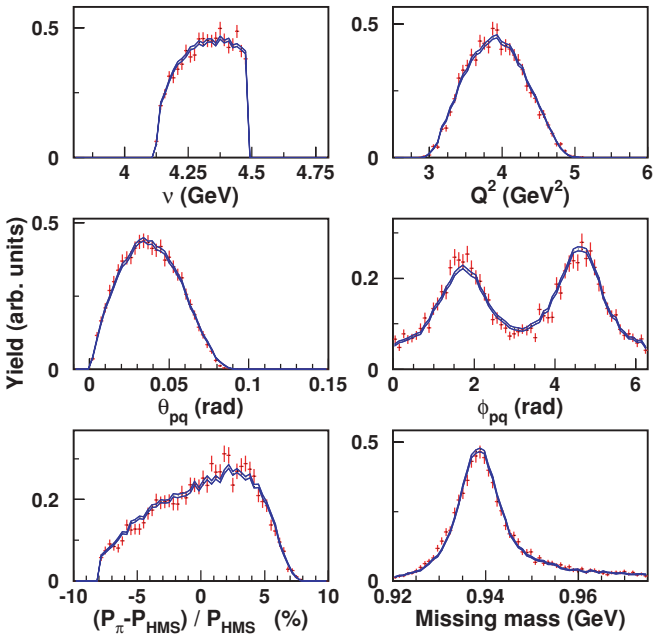

FIG. 3. (Color online) Experimental (crosses) and Monte Carlo (lines) distributions for the hydrogen target at $Q^2 = 3.91$ GeV ^{2}.

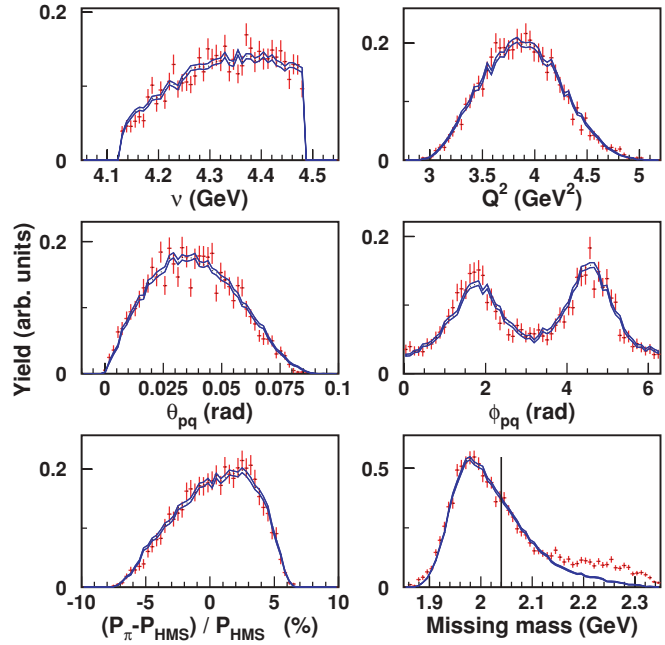

FIG. 4. (Color online) Experimental (crosses) and Monte Carlo (lines) distributions for the deuterium target at $Q^2 = 3.91$ GeV^2. The vertical line in the bottom right panel shows the position of the two-pion production missing-mass cut.

A. Monte Carlo simulation

The standard Hall C Monte Carlo simulation code, SIMC, was used to simulate the experiment. Events were generated over a phase space marginally larger than the acceptance of the spectrometers. After events were generated at the reaction vertex, they were propagated through the spectrometers using transformation matrices that were determined from a COSY INFINITY [37] model of the spectrometers and optimized using a set of calibration data. Each event was weighted by the relevant model cross section (see Sec. VII A2). A comparison between experimental and simulated distributions of reconstructed quantities for a hydrogen target are shown in Fig. 3. If the detector setup and the spectrometer acceptances (including coincidence acceptance) are realistically modeled in the simulation, the boundaries of the distributions should match. Differences in magnitude can be attributed to differences between the actual cross section and the one used in the model.

To describe electroproduction from nuclear targets, the quasifree approximation was used, because the energy of the incoming electron is large compared to the energy associated with the binding of the nucleons. The properties of the nucleons inside the nucleus were assumed to be described by an independent particle shell model, where each nucleon interacts with a mean field exerted by the other nucleons. The probability of finding a nucleon with momentum $\mathbf{p}_m$, and separation energy E_m, in the nucleus is given by a spectral function, $S(E_m, \mathbf{p}_m)$. Previously constructed spectral functions were used for deuterium, carbon, gold [16,17], and aluminum [38]. The copper spectral function was constructed from the iron spectral function described in Ref. [39] by increasing the number of protons in the outermost $1f$ shell from six to nine and by changing the central binding energy of this shell using the separation energy for copper. The spectral functions did not include any corrections to account for shifts in their strength owing to large missing momentum caused by nucleon-nucleon correlations.

Although, in the quasifree approximation the momentum of the struck proton is taken to be $\mathbf{p}_m$, the energy E_m is not constrained by any of the assumptions in the quasifree approximation. In the present analysis, the off-shellness of the proton was described by

$$M_A = M_p + M^*_{A-1},$$
$$E_p = M_A - \sqrt{(M^*_{A-1})^2 + |\mathbf{p}_m|^2}, \quad (11)$$

where M_A is the nuclear mass, M_p is the mass of the nucleon, M^*_{A-1} is the mass of the spectator nucleons, which include the off-shellness, and E_p is the energy of the struck proton. Comparisons between experimental and simulated distributions of reconstructed quantities for nuclear targets are shown in Figs. 4, 5, 6, and 7. In addition, two other methods of accounting for off-shell effects were tried in the analysis. The first one, called the "proton-on-shell" model, assumes that the proton was on the mass shell before the interaction. Thus, $E_P = \sqrt{|\mathbf{p}_m|^2 + M_p^2}$. The second one assumes that the invariant masses of the spectator nucleons are the same immediately before and after the interaction [40]. Thus, $E_m = M_p + M^*_{A-1} - M_A$ and $E_p = M_A - \sqrt{(M^*_{A-1})^+ \mathbf{p}_m^2}$. All three models were compared with the data and the first method described was found to provide the best description of the data.

The radiative corrections used in this analysis were based on the formalism of Ref. [41], which was explicitly modified and improved for $(e,e'p)$ coincidence reactions in Ref. [42]. It

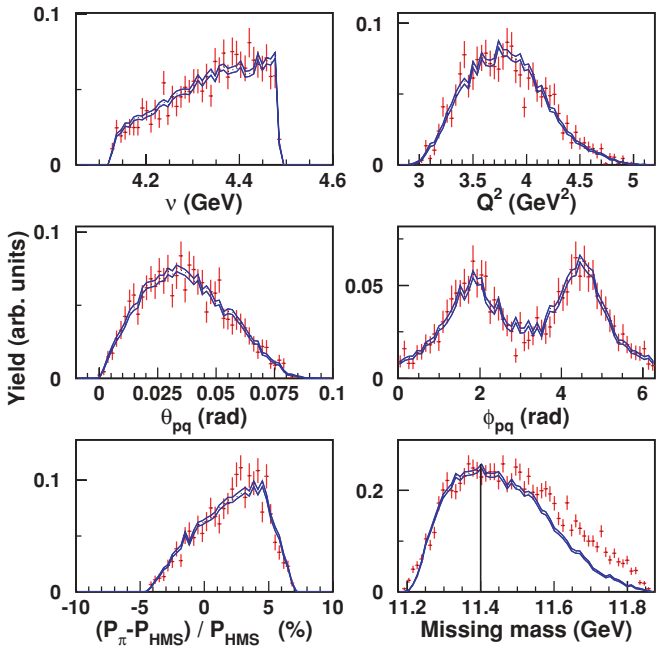

FIG. 5. (Color online) Experimental (crosses) and Monte Carlo (lines) distributions for the carbon target at $Q^2 = 3.91$ GeV^2. The vertical line in the bottom right panel shows the position of the two-pion production missing-mass cut (see Sec. VII A4 for discussion).

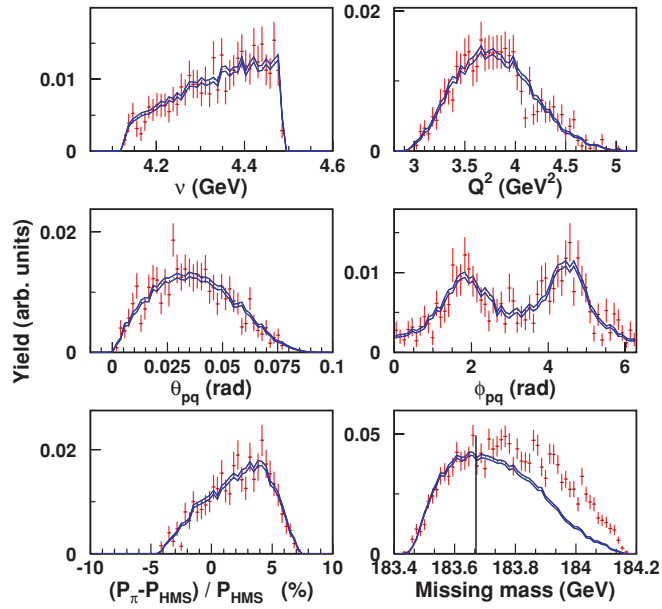

FIG. 7. (Color online) Experimental (crosses) and Monte Carlo (lines) distributions for the gold target at $Q^2 = 3.91$ GeV^2. The vertical line in the bottom right panel shows the position of the two-pion production missing-mass cut (see Sec. VII A4 for discussion).

includes both external and internal radiation. The formalism was further modified for pion electroproduction, where the target particle is assumed to be a stationary proton, while

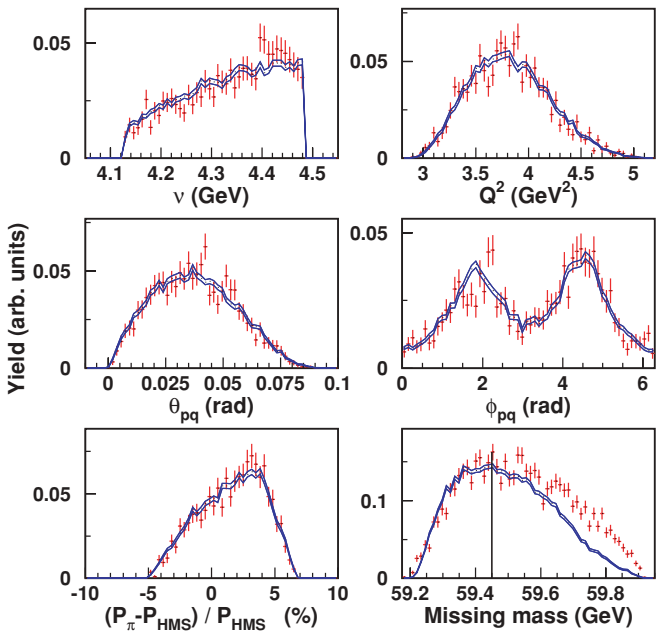

FIG. 6. (Color online) Experimental (crosses) and Monte Carlo (lines) distributions for the copper target at $Q^2 = 3.91$ GeV^2. The vertical line in the bottom right panel shows the position of the two-pion production missing-mass cut (see Sec. VII A4 for discussion).

the final pion is assumed to be off shell. The assumption of off-shellness was tested in the simulation by trying different treatments of off-shellness and was found to change the Monte Carlo yield by at most 0.5%. The largest source of uncertainty in the simulation of radiative processes comes from radiation owing to the pion, as the electron radiation is relatively well modeled. The simulated yield changed by 2%–4% when radiation from the pion was turned off, depending on A and Q^2 (2% for low Q^2 settings and 4% for the heavy targets at high Q^2). From these studies, we assume a normalization uncertainty owing to radiative corrections of 2%.

SIMC incorporates the effects of the pion decay [40], multiple scattering, and energy loss. Pions may decay in flight into μ^+ and $\bar{\nu}_\mu$ before they are detected in the HMS detector hut. Typically, the pion momentum was always greater than 2 GeV/c, so the laboratory frame lifetime of the pion was at least 0.37 μs. The time required to travel from the target to the HMS hut was $\sim$0.083 μs and, at the lowest pion momentum setting, about 20% of the pions were expected to decay in flight. Pion events could not be separated experimentally from muon events, and so pions that did decay could still produce a valid trigger and fall inside the experimental acceptance. Therefore, the path of the pion was divided into steps (the distances between apertures in the HMS Monte Carlo), and the decay of the pion was simulated at each step. If the pion decayed in a given step, then the muon kinematics were generated (the muon was produced mostly at forward angles) and the muon was transported through the spectrometer. Because the central momentum of the HMS was not changed between target changes, the pion decay correction was the same for the heavy targets and the hydrogen target, and they cancel in the ratio

of yields. This is also true for the L-T separation analysis, where the HMS central momentum settings are not very different between the high and low ϵ settings. The systematic uncertainty owing to pion decay comes from events where the pion decayed inside either a quadrupole or a dipole in the HMS. These events are not modeled very well by the spectrometer optics model. For the present analysis, 2.5% (1.4%) of the pion decays occur inside the spectrometer at the lowest (highest) Q^2 setting. The random uncertainty is about 0.5%, owing to muons coming from pions outside the spectrometer acceptance. The difference between targets is smaller than 0.1%. SIMC also takes into account pions that punched through the spectrometer collimator; simulation of such events was based on a calculation of the pion transmission through materials described in Ref. [36].

SIMC was modified to take into account the effect of Pauli blocking. In the ideal Fermi gas model, nucleons occupy all single-particle states with momentum k less than the Fermi momentum k_F. In the π^+ electroproduction channel, the π^+ are produced from protons in the nuclear targets. The reaction will produce a recoiling neutron, which is forbidden to occupy any single-particle state that already contains a neutron. In the ideal Fermi gas model, this is equivalent to the requirement that the recoiling neutron momentum, k_n, must be greater than k_F. In the presence of short-range correlations, some of the single-particle states below the Fermi momentum will be depleted while populating the states above the Fermi momentum. The correction for this effect is obtained by assigning a weight of $1 - n(k_\pi)$ to each Monte Carlo event, where $n(k_\pi)$ is the distribution function of Fantoni and Pandharipande [43] calculated using perturbation theory in a correlated basis.

Final-state interactions between the knocked-out neutron and the residual nucleons (n-N FSI) can affect the quasifree cross section and can shift strength in the missing-mass spectrum toward the single pion production threshold. It is likely to have the strongest effect when the relative momentum between the recoiling neutron and the spectator nucleons is small. An earlier experiment on light nuclei at Jefferson Lab showed that the effect of n-N FSI on the quasifree cross-section reduces with increasing Q^2 [40]. Because this experiment was conducted at relatively high Q^2, n-N FSI were not explicitly accounted for in the simulation. The lack of full accounting of the n-N FSI is most likely to be the cause of the discrepancy in the shape of the missing-mass spectrum at the lowest $Q^2 = 1.1$ GeV^2 setting, seen in Figs. 8 and 9.

Coulomb corrections to the incoming and scattered electron are applied according to the effective momentum approximation (EMA) approach [44]. This approach includes an improvement over earlier versions of the EMA, using an average potential to account for the focusing of the incoming electron wave function [44]. No Coulomb corrections were applied to hydrogen and deuterium, because this effect is already included in the elementary pion cross sections. The corrections for the copper target are between 0.2% and 2%, while the yield corrections for the gold target range between 0.9% and 4.4%. We assume that 25% of this correction contributes to the uncorrelated uncertainty.

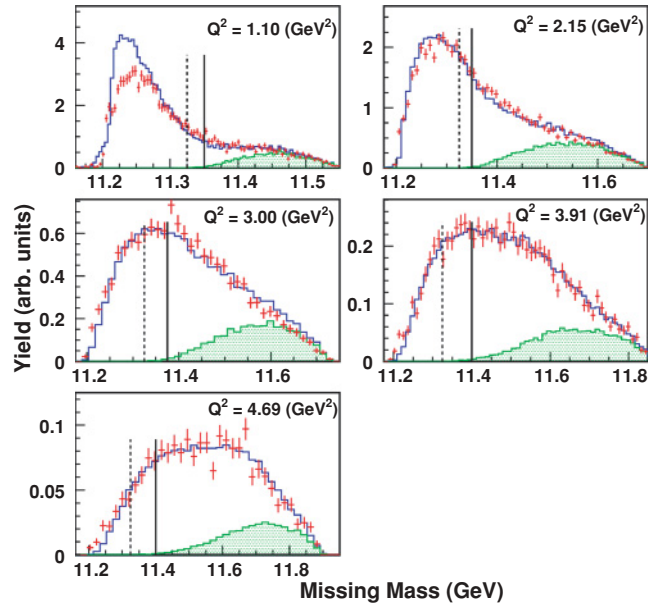

FIG. 8. (Color online) Nuclear missing-mass distributions (in GeV^2) for ^{12}C$(e,e'\pi^+)$. The data (red crosses) are compared to the simulation (blue line), which is a sum of single-pion and multiple-pion simulations. The shaded areas (green) shows the contributions from the multipion simulation. The full simulation is normalized to the data. The dashed vertical lines represent the threshold for double-pion production (11.34 GeV^2). The solid vertical lines represent the position of the cut used in this analysis.

1. *Detector acceptances in SIMC*

The acceptances for both spectrometers were studied by comparing data and simulated distributions for reconstructed quantities like Q^2, t, and missing mass, as shown in Fig. 3. The acceptance uncertainties were estimated using the over-constrained H$(e,e'p)$ reaction. These uncertainties arise from the uncertainty in the knowledge of the momentum and angle settings of the spectrometers and the beam energy. The point-to-point yield variation was found to be 1% for different Q^2 values.

2. *The model cross section*

The Monte Carlo simulation was used to extract the bin-centered experimental cross section by iterating the model cross section until the simulated distributions matched those of the data. The starting model was based on previous hydrogen pion electroproduction data from Hall C [36]. The model cross section was taken as the product of a global function describing the W dependence times (a sum of) Q^2 and t- and θ-dependent functions for the different structure functions. A correction function, which was assumed to factorize,

$$C_H(W, Q^2, t, \phi_{pq}) = O(W)K(Q^2)T(t)F(\phi_{pq}), \quad (12)$$

was determined by iterating the model and comparing it to hydrogen elementary cross sections. These correction functions were assumed to be second-order polynomials, with the exception of $F(\phi_{pq})$, which was assumed to be of third order.

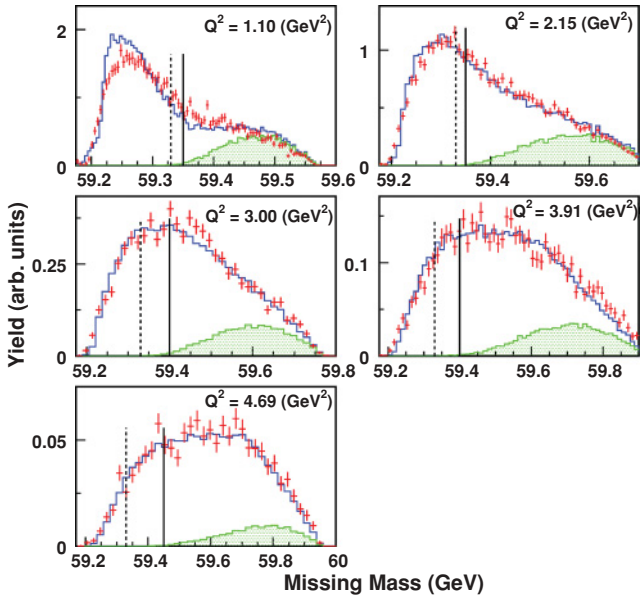

FIG. 9. (Color online) Nuclear missing-mass distributions (in GeV^2) for ^{63}Cu$(e,e'\pi^+)$. The data (red crosses) are compared to a sum of single-pion and multiple-pion simulations (blue lines). The shaded areas (green) show the contributions from the multipion simulation. The full simulation is normalized to the data. The dashed vertical lines represent the threshold for double-pion production (59.33 GeV^2). The solid vertical lines represent the position of the cut used in this analysis.

3. *Iteration procedure*

For the hydrogen target, the bin-centered experimental cross section is given by

$$\left(\frac{d^5\sigma_A}{d\Omega_{e'}dE_{e'}d\Omega_\pi}\right)^{\rm exp}_{x_0} = \frac{Y_{\rm data}}{Y_{\rm MC}}\left(\frac{d^5\sigma_A}{d\Omega_{e'}dE_{e'}d\Omega_\pi}\right)^{\rm model}_{x_0}. \quad (13)$$

For nuclear targets, the bin-centered experimental cross section is given by

$$\left(\frac{d^6\sigma_A}{d\Omega_{e'}dE_{e'}d\Omega_\pi dP_\pi}\right)^{\rm exp}_{x_0} = \frac{Y_{\rm data}}{Y_{\rm MC}}\left(\frac{d^6\sigma_A}{d\Omega_{e'}dE_{e'}d\Omega_\pi dP_\pi}\right)^{\rm model}_{x_0}, \quad (14)$$

where the subscript, x_0, indicates that the cross section is evaluated at a particular point (W_0, Q_0^2, θ_0) inside the acceptance. The model cross sections for hydrogen and for the nuclear targets were determined using a point-target Monte Carlo simulation, which was performed using scattered electron kinematics and pion angles generated randomly within a very narrow phase space volume that corresponded to W_0, Q_0^2, and θ_0. For nuclear targets, P_π was generated over the whole phase space from which a narrow range was selected in the analysis.

The extracted cross sections depend on the initial cross-section model, and thus there are systematic uncertainties associated with it. This uncertainty was obtained by extracting the cross section using a different starting model and was found to be 1.1%. However, this uncertainty will not contribute to nuclear transparency, because the nuclear transparency involves the ratio of two Monte Carlo yields.

4. *Multipion production in nuclear targets*

In the kinematics of this experiment, single-pion production dominates. The production of more than one pion in a single event (multiple pion production) was suppressed for hydrogen target during the pionCT experiment owing to the relatively high $Q^2 > 1$ GeV^2 and $W > 2.1$ GeV above the resonance region. This suggests that the mechanism for multiple-pion production involves the outgoing pion producing one or more pions from a nucleon in a second process that is incoherent from the production of the first pion. Multiple-pion events can only be produced above a missing-mass threshold that is larger than the missing-mass threshold for single-pion production, that is, $M_x = M_{A-1} + M_\pi$ for a nucleus of mass A. Indeed, in the analysis, at first a missing-mass cut exactly corresponding to this threshold was used to suppress multiple-pion events. However, this cut resulted in an unacceptable loss of statistics at the highest Q^2 settings, and thus an alternative cut on the nuclear missing mass above the multipion threshold was used.

To describe events above the two-pion threshold, a multiple-pion production simulation was developed for the nuclear target analysis. The mechanism for multiple-pion production was assumed to be quasifree single-pion production from a nucleon followed by a secondary process that was incoherent from the first, where the pion produced one or more pions from a different nucleon. The cross section for the secondary process was assumed to be uniform over the acceptance of the HMS spectrometer.

The effect of multipion production can be seen in Figs. 8 and 9 for the carbon and copper targets. The agreement between the missing-mass distributions obtained from data and simulation improves with increasing Q^2. The discrepancy seen at $Q^2 = 0.1$ GeV^2 is attributed to the reaction mechanisms missing from the simulation, such as final-state interactions between the knocked-out neutron and the residual nucleons (nN-FSI) and short range correlations. The effect of these reaction mechanisms decrease with increasing Q^2.

These results show that it is safe to increase the double-pion missing-mass cut above the threshold with minimal contamination. The double-pion missing-mass cut was placed at the position where the systematic uncertainty from the contribution of multiple-pion events was less than 5%. With these cuts, the total uncertainty owing to multipion contamination is <0.4%. We also noted an interesting smooth A dependence in the ratio of the multiple-pion to single-pion yields.

5. *Test of the quasifree assumption*

The average cross sections were extracted by integrating over the whole acceptance (W, Q^2, and t). This averaging reduces the systematic uncertainties related to the cross-section model in the Monte Carlo by smearing the exact kinematic information of the extracted cross section. We bin the data in ϕ by integrating over all other kinematic variables at each ϵ setting. The azimuthal angular coverage for the hydrogen target at $Q^2 = 2.15$ GeV^2 can be found in Fig. 10. Owing to correlations in the kinematics, the central W, Q^2, and t values for each ϕ bin are different from those obtained by integrating over the entire ϕ region. Thus, a Monte Carlo

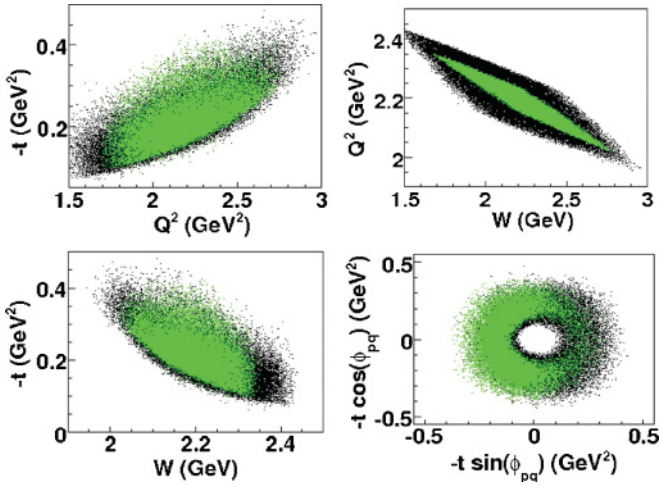

FIG. 10. (Color online) The plot in the top left panel is the phase space comparison between the high (black) and low (green) ϵ for $-t$ vs Q^2. The plot in the top right panel is the phase space comparison for W vs Q^2. The plot in the bottom left panel shows the comparison for $-t$ vs W. The bottom-right panel shows the azimuthal coverage for these two data sets.

simulation is used to account for the correction between the cross section evaluated at the center of each ϕ bin and the one for the entire ϕ region. The four structure functions in Eq. (8) are extracted by fitting the data with respect to ϕ for both high and low ϵ settings simultaneously. A representative fit for the hydrogen target at $Q^2 = 2.15$ GeV^2 can be found in Fig. 11. In the analysis, an additional acceptance cut is used to ensure that the kinematic region given by W, Q^2, and t is the same at high and low ϵ. Such a phase space comparison is shown in Fig. 10.

The same fitting procedure described above could be used to obtain the Rosenbluth-separated pion electroproduction cross

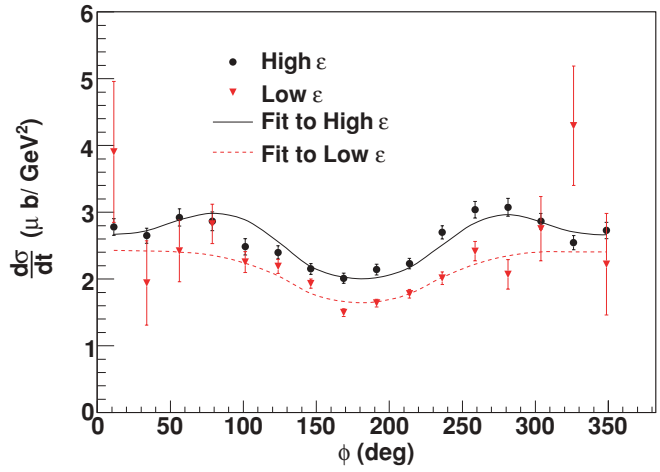

FIG. 11. (Color online) Representative plot of the experimental cross sections, $\frac{d^2\sigma}{dtd\phi}$ as a function of the azimuthal angle ϕ at $Q^2 = 2.15$ GeV^2 for high and low ϵ. The curves shown represent the fits of the measured values of the cross section to Eq. (8). The $-t$ in this plot correspond to the common region between the high and low ϵ data shown in Fig. 10. Only the statistical uncertainties are shown.

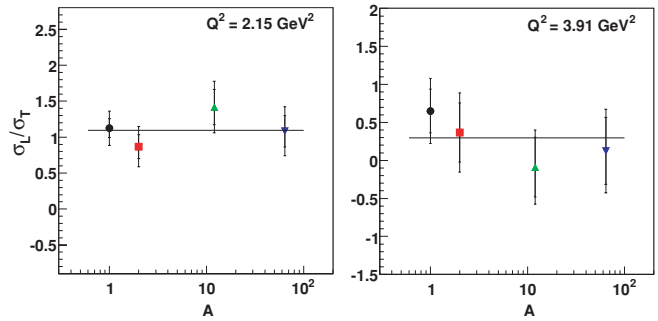

FIG. 12. (Color online) The ratios of longitudinal to transverse cross sections for pion electroproduction from ^{1}H, ^{2}H, ^{12}C, and ^{63}Cu targets at fixed $Q^2 = 2.15$ (left) and 3.91 (right) GeV^2. The inner error bars represent the statistical uncertainties, while the outer error bars are the sum in quadrature of the statistical and systematic uncertainties. The curves represent constant-value fits to all nuclear data at a fixed Q^2. The probabilities of these constant-value fits, assuming Gaussian statistics, is 69% and 70%, respectively. The statistics at $Q^2 = 3.91$ GeV^2 are limited, and the statistical uncertainties for carbon and copper targets are larger than 50%.

sections. However, while this separation is relatively straightforward for a hydrogen target, a similar separation for nuclear targets relies on the assumed quasifree reaction mechanism. This is because beyond the W, Q^2, and t dependence, the elementary off-shell pion electroproduction cross section has a P_π dependence in the nuclear medium. The quasifree P_π dependence, which is taken into account in the Monte Carlo simulations for the nuclear targets, is used as a starting model. Then the iterative procedure described earlier is followed. This implies that the extracted nuclear cross sections represent the averaged values integrated over a wide kinematic acceptance, rather than the bin-centered values. These averaged cross sections are used to obtain the longitudinal-to-transverse ratios between nuclear and hydrogen targets. The ratios of longitudinal-to-transverse cross sections at fixed $Q^2 = 2.15$ and 3.91 GeV^2 for the various targets used in this experiment are shown in Fig. 12. We find no difference, within the experimental uncertainties, between the ratios of longitudinal to transverse cross sections for nuclear and hydrogen targets; this can be viewed as a confirmation of the quasifree reaction mechanism.

VIII. SYSTEMATIC UNCERTAINTY STUDIES

Table III lists the systematic uncertainties associated with the extraction of the nuclear transparencies. Several sources of these uncertainties were discussed in Secs. VII A1–VII A4.

The uncertainty in the acceptance is based on extensive single-arm elastic and deep-inelastic measurements from Refs. [45,46] and ^{1}H$(e,e'p)$ data, including sieve-slit data on a carbon target, taken to check the optical matrix elements. The influences of the uncertainties in the offsets in the kinematical variables such as beam energy, momenta, and angles were determined by changing their values by their uncertainties and evaluating the resultant changes in the cross sections.

TABLE III. The systematic uncertainties in extracting the nuclear transparencies. The uncorrelated uncertainties contribute directly to the point-to-point uncertainties in the nuclear transparencies, the A-dependent uncertainties are independent of Q^2, while the correlated uncertainties are independent of both the target nucleus and Q^2.

Item	Uncorrelated uncertainty (%)	A dependent (%)	Correlated uncertainty (%)
HMS Čerenkov	0.2		0.3–0.5
SOS Čerenkov	0.2		0.3–0.5
Charge	0.4–0.9		0.4
Coincidence blocking	0.2		
HMS trigger	0.5		
Dead time	0.2–0.5		
HMS tracking	1.0		1.0
SOS Trigger	0.5		
SOS Tracking	0.5		0.5
Pion decay	0.1		1.0
Coulomb corrections	<1.0		
Radiative corrections	1.0–2.0		2.0
Collimator	0.5		1.0
Acceptance	1.0		2.0
Iteration procedure	1.1		
Multipion contamination	<0.4		
Target thickness		0.5–1.0	
Pion absorption		0.5	2.0
Total	2.4–3.4	0.7–1.1	3.9–4.0
Model dependence	3.5–7.6		

The uncertainty in the solid-target thickness is dominated by the knowledge of their purities and thicknesses. For the 4-cm liquid targets, the uncertainty is dominated by the target boiling correction and the beam path length because the beam does not pass exactly through the axis of the liquid target cylinder. The uncertainty in the total charge includes a 0.4% uncertainty in the calibration of the beam current monitors.

The largest correlated systematic uncertainties are radiative corrections and acceptance, resulting in a total correlated uncertainty of 3.9%–4.0%. The uncorrelated systematic uncertainty is dominated by contributions from the acceptance, radiative corrections, and the iteration procedure, resulting in a total uncorrelated uncertainty of 2.4%–3.4%. The largest contribution to the "A-dependent" uncertainty is the target thickness, resulting in a total uncertainty of 0.7%–1.1%.

The largest source of uncertainty in the radiative correction procedure comes from pion radiation, as the electron radiation is relatively well known. The Monte Carlo equivalent yields changed by 2%–4% when pion radiation was turned off (2% at low Q^2 and 4% for the heavy targets at high Q^2). From this, the normalization uncertainty was taken to be 2%. The point-to-point uncertainty in the radiative corrections was estimated from the target dependence of the change in Monte Carlo equivalent yield when the pion radiation was turned off. This was 1% at the low Q^2 and 2% at high Q^2.

TABLE IV. The systematic uncertainties in extracting cross sections and in extracting the ratios of the longitudinal to transverse cross sections.

Item	Uncertainty in differential cross section (%)	Uncertainty in L-T cross section ratio (%)
HMS Čerenkov	0.4–0.5	
SOS Čerenkov	0.4–0.5	
Charge	0.6–1.0	
Coincidence blocking	0.2	
HMS trigger	0.3–0.5	
Dead time	0.2–0.5	
HMS tracking	1.1–1.4	
SOS trigger	0.3	
SOS tracking	0.5	
Pion decay	1.0	
Coulomb corrections	<1.0	
Radiative corrections	2.2–2.8	
Collimator	1.1	
Acceptance	2.2	
Iteration procedure	1.3–1.5	13.0–18.0
Multipion contamination	<0.4	
Target thickness	0.5–1.0	
Pion absorption	2.1	
Kinematics	1.5–2.0	3.0–16.6
Momentum coverage		<12.0
Total	4.8–5.7	

In addition to these uncertainties, a Q^2-dependent model uncertainty was determined to be 3.5%–7.6%. This uncertainty is the quadrature sum of the change in Q^2 dependence of the transparency when using two different spectral functions and two different Fermi distributions in the simulation and the Q^2-dependent uncertainty arising from reactions mechanisms that are not included in the simulation (such as n-N FSI). The latter was estimated by quantifying the difference in shape of the missing-mass spectra between data and simulation.

Table IV lists the systematic uncertainties in extracting the unseparated cross sections and the uncertainty in extracting the ratio of longitudinal to transverse cross section. These were obtained using the quadrature sum of the correlated, uncorrelated, and A-dependent uncertainties along with two additional sources of uncertainty labeled as "kinematics" and "momentum coverage." The "kinematics" part represents the uncertainties in the knowledge of spectrometer angles and momentum setting. It will not contribute to the nuclear transparency because the spectrometer settings are exactly the same for different targets. The "momentum coverage" part represents the effect of the wider momentum cut (to obtain enough statistics in the low-ϵ region) used in the Rosenbluth separation.

IX. RESULTS AND DISCUSSION

The differential cross sections for hydrogen are shown in Fig. 13 and those for all four nuclear targets (deuterium, carbon, copper, and gold) are shown in Fig. 14. All numerical

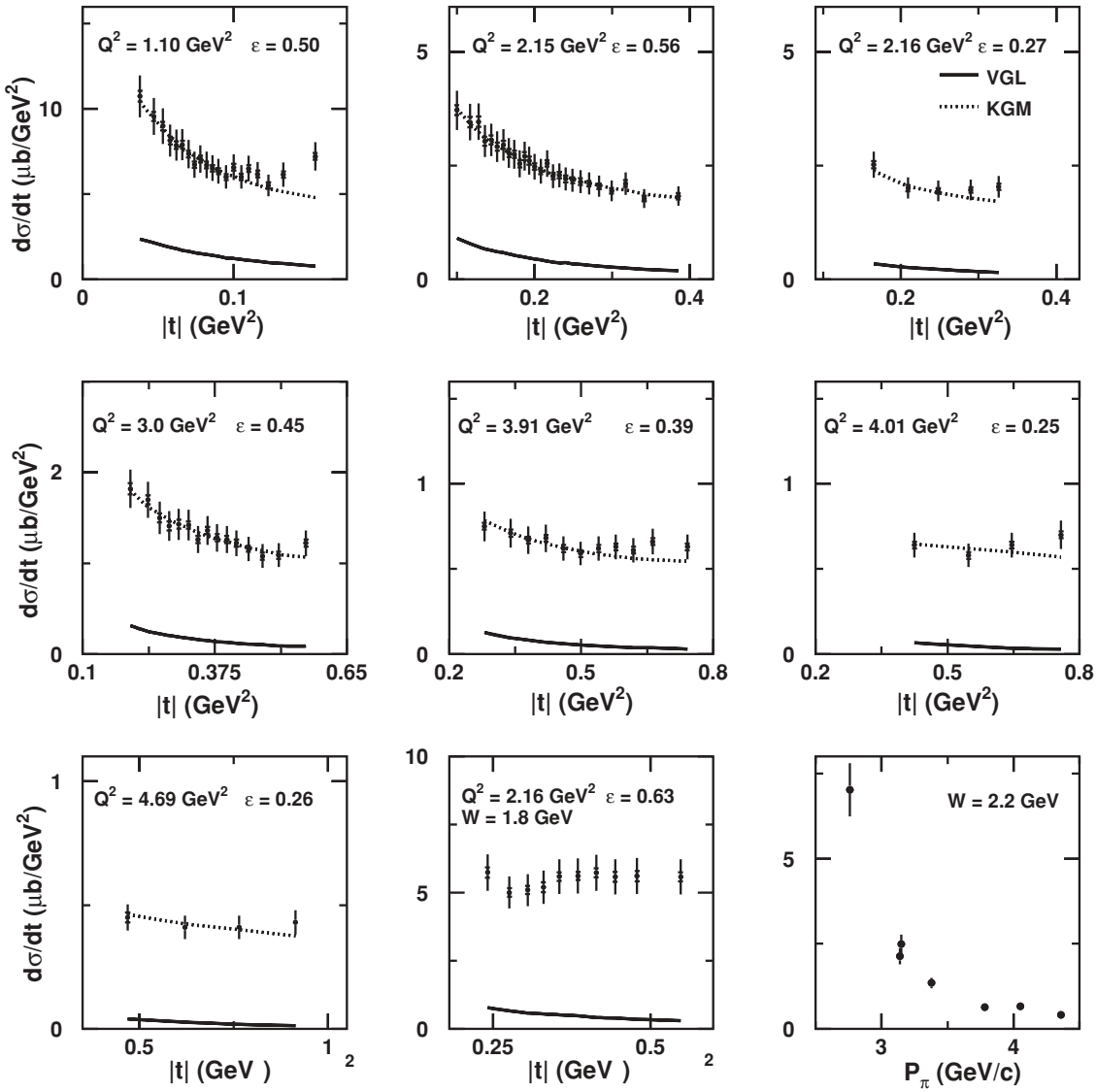

FIG. 13. Differential cross sections $\frac{d\sigma}{dt}$ for pion electroproduction from hydrogen versus $|t|$. The last panel (bottom right) shows the differential cross section versus the pion laboratory momentum (only the seven $W = 2.2$ GeV points are shown here). For each of the points shown in the cross section versus pion momentum plot (last panel), the data were averaged over the respective t ranges shown in the previous panels. For the panels showing the differential cross section versus $|t|$, the center of mass energy is $W = 2.2$ GeV for all except one kinematic setting, where $W = 1.8$ GeV (bottom middle). The inner error bars represent the statistical uncertainties, while the outer error bars are the sums in quadrature of the statistical and systematic uncertainties. The data are compared with both the VGL-Regge [47] and the KGM [48] calculations where available (see text).

values are tabulated in Appendices A and B (tables VI–XII). In the following sections, the global dependencies of the hydrogen and nuclear cross sections are reviewed and the data are compared to recent model calculations. The results of the quasifree reaction mechanism test and the extracted nuclear transparencies are also shown.

A. Global dependencies and model comparison for hydrogen

For the different values of Q^2, the differential cross section shows the characteristic falloff with $-t$, owing to the pion pole in σ_L. The magnitude of the cross section at constant W decreases with increasing $-t$ and Q^2, mostly because the value of $-t_{\min}$ increases with Q^2. In Fig. 13 (bottom right panel), we show the differential cross section vs pion laboratory momentum (P_π). In this plot, each point at a particular P_π represents the differential cross section averaged over the $|t|$ range shown in the one of the other panels of Fig. 13 that corresponds to the Q^2 value at that P_π (see Table I).

The cross sections are compared to predictions of two different models of pion electroproduction, the VGL-Regge model [47] and the more recent "KGM" model [48]. The VGL-Regge model is a gauge-invariant calculation incorporating π and ρ Regge trajectory exchanges. It significantly underestimates the measured differential cross sections. Most of the discrepancy can likely be attributed to the model

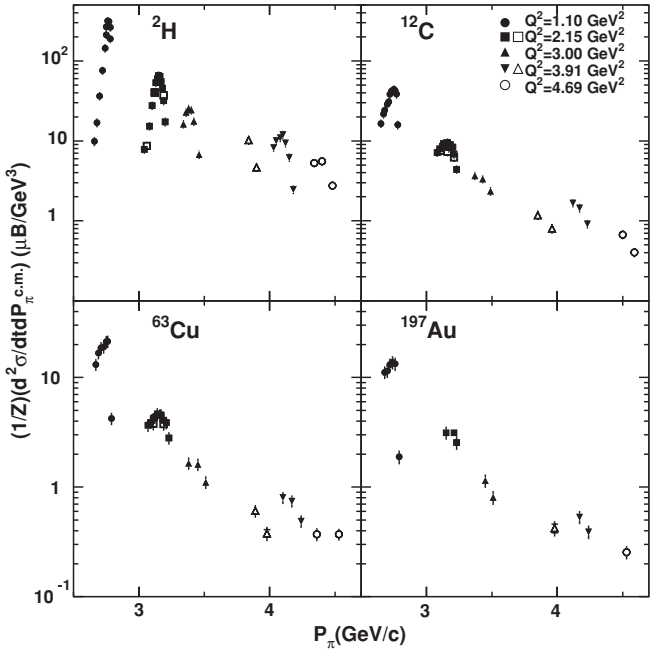

FIG. 14. The extracted doubly differential cross sections, $\frac{1}{Z}\frac{d\sigma}{dtdP_\pi^{\text{c.m.}}}$, versus the pion momentum P_π in the laboratory frame for the deuterium, carbon, copper, and gold targets, respectively. The cross sections are normalized by Z because in the quasifree approximation an exclusive π^+ can only be generated from a proton. The inner error bars represent the statistical uncertainties, while the outer error bars are the sums in quadrature of the statistical and systematic uncertainties. For each target at $Q^2 = 2.15$ GeV^2 and $Q^2 = 3.91$ GeV^2, the solid symbols represent the high-ϵ kinematics while the open symbols represent the low-ϵ kinematics.

underestimating the transverse part of the cross section, as shown in Ref. [49], while the agreement with σ_L data is much better. The KGM model [48] agrees much better with the measured differential cross sections. It includes a deep-inelastic scattering (DIS) ansatz for the transverse part of the cross section, while the longitudinal cross section is dominated by hadronic degrees of freedom and the pion electromagnetic form factor.

B. Global dependencies for nuclear targets

We have extracted the differential cross sections for all four nuclear targets (deuterium, carbon, copper, and gold) at the eight different kinematics settings given in Table I. Here, the additional complication owing to the added degree of freedom induced by the Fermi-motion (or nuclear binding) of the struck proton is taken into account by extracting doubly differential cross sections, $\frac{d^2\sigma}{dtdP_\pi^{\text{c.m.}}}$, where $P_\pi^{\text{c.m.}}$ is the pion momentum in the center-of-mass frame of the virtual photon and the nucleus.

The local variations in the nuclear cross sections, as illustrated in Fig. 14, indicate effects owing to Fermi motion. These local variations are more pronounced for the deuterium target, because of its narrower Fermi cone. Although the general trend of the nuclear cross sections are similar to those of the hydrogen cross sections, the falloff of the nuclear cross sections with increasing P_π is steeper than that of the hydrogen cross sections.

C. Verification of the quasifree mechanism

A prerequisite for an interpretation of nuclear transparency as a function of Q^2 is that the reaction mechanism remain identical over the Q^2 range. This translates into an important condition in searching for CT using pion electroproduction: The reaction should proceed through a quasifree mechanism.

There are many mechanisms that could break down the quasifree assumption, such as:

(i) *Nucleon-nucleon (NN) final-state interactions.* The amplitude of NN final-state interactions can interfere with the elementary electropion production amplitude, causing a change in the ratio of the longitudinal to the transverse cross section. For example, the disagreement in the missing-mass spectra between data and simulation at $Q^2 = 1.1$ GeV^2 (Figs. 8 and 9) is expected to be attributable to such effects and other potential reaction mechanism effects not included in the Monte Carlo model. The agreement between data and Monte Carlo at higher values of Q^2, however, suggests only a small contribution from such NN final-state interactions.

(ii) *Rescattering.* Rescattering involves the electroproduction of a meson followed by a secondary interaction that produces the detected π^+ particle. For example, such rescattering contributions have been shown to dominate the cross section in ρ^0 photo-production for $t \geqslant 0.5\,\text{GeV}^2$ [50]. In principle, if the rescattering effect dominates, one would expect a modification of both the longitudinal-to-the-transverse cross-section ratio, and the cross-section dependence on W.

(iii) *Pion excess.* Excess pions may be present in a nuclear system owing to the long range of meson-exchange currents [51]. If such pion excess effects are significant, one would anticipate a change in the ratio σ_L/σ_T of the measured nuclear cross sections as compared those of to the hydrogen cross sections. An earlier experiment on light nuclei at low Q^2 did not find any pion excess [52].

(iv) *Medium modification of nucleons.* The European-Muon Collaboration discovered [53] that the structure functions for deep inelastic inclusive lepton scattering off nuclear targets differ from those from deuteron targets. Although the effect remains poorly understood, it is generally accepted that nucleon structure will be modified within a nuclear medium owing to nuclear binding and non-nucleonic QCD effects. Such nucleon medium modifications could also impact the nuclear pion electroproduction cross sections, but they are generally expected to also lead to a change in the ratio of longitudinal to transverse pion electroproduction cross sections, σ_L/σ_T.

(v) *Two-nucleon correlations.* A series of $A(e,e'p)$ measurements revealed that the spectroscopic factors for proton valence shells were quenched by approximately 30%–35% compared to mean-field expectations [54,55]. A possible explanation for this discrepancy is that correlations move some of the single-particle

strength to orbitals above the Fermi energy. This kind of correlation will change the nuclear spectral function and thus break down the quasifree assumption.

The most straightforward verification of the quasifree mechanism is the equivalence of the longitudinal-transverse character for pion electroproduction from nuclear and hydrogen targets. The ratio of longitudinal to transverse cross sections should, for instance, be independent of the nuclear atomic number A. The ratios of longitudinal to transverse cross sections at fixed $Q^2 = 2.15$ and 3.91 GeV^2 for the various targets are shown in Fig. 12.

The σ_L/σ_T ratios are independent of A within the experimental uncertainties and are thus consistent with the quasifree assumption. However, they cannot rule out non-quasifree reaction mechanism effects that affect the longitudinal and transverse character of pion electroproduction in a similar fashion, for instance, NN final-state interaction, rescattering, pion excess, or medium modification effects. Note that we have intentionally kept the value of $-t$ of the measurements low ($\leqslant$0.5 GeV^2) to minimize complications owing to rescattering or two-nucleon effects. Together with the overall good agreement between data and Monte Carlo simulations, we have gained confidence in the validity of the quasifree reaction mechanism beyond $Q^2 = 1.1$ GeV^2.

D. Nuclear transparencies

As mentioned earlier, nuclear transparency is defined as the ratio of the cross section per nucleon for a process on a bound nucleon inside a nucleus to that from a free nucleon. The P_π dependence of the nuclear transparencies for various nuclei are shown in Fig. 15.

Before we discuss the various model calculations, we first redefine the nuclear transparency (T_D) as the cross sections of heavy nuclear targets as compared to those of a deuterium target. This reduces the uncertainty owing to the unknown elementary pion electroproduction off a neutron and uncertainties in the Fermi smearing corrections. The results are shown in Fig. 16, where we present the data versus Q^2 rather than pion momentum P_π. As expected, the results are not too different because the deuterium nuclear transparencies are close to unity, as shown in top left panel of Fig. 15. We note, in addition, that the deuterium nuclear transparency is found to be independent of P_π, with 81% probability, while the probabilities of the transparency being independent of P_π for carbon, aluminum, copper, and gold are 11.6%, 14.3%, 1.9%, and 3.6%, respectively. The nuclear transparency results are tabulated in Appendix C.

The nuclear transparencies are expected to be near constants over the pion momentum range of the experiment from a traditional nuclear-physics point of view [23] because the hadron-nucleon cross sections are nearly independent of momentum over the range of momenta in Figs. 15 and 16. Instead, the observed pion nuclear transparency results (as compared to both hydrogen and deuterium cross sections) show a slow but steady rise versus pion momentum for the nuclear ($A > 2$) targets, causing a deviation from calculations without CT.

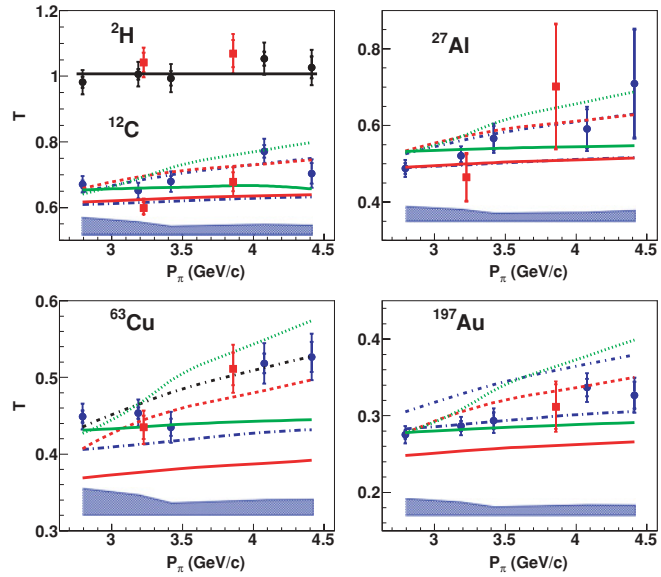

FIG. 15. (Color online) Nuclear transparency, T, vs P_π for ^{2}H and ^{12}C, ^{27}Al, ^{63}Cu, and ^{197}Au. The inner error bars are the statistical uncertainties and the outer error bars are the statistical and point-to-point systematic uncertainties added in quadrature. The solid circles (blue) are the high-ϵ points, while the solid squares (red) are the low-ϵ points. The dark (blue) bands are the model uncertainties (for details, see Sec. VIII). The dashed and solid lines (red) are Glauber calculations from Larson *et al.* [9], with and without CT, respectively. Similarly, the dot-short dash and dot-long dash lines (blue) are Glauber calculations with and without CT from Cosyn *et al.* [56]. The effects of short-range correlations are included in these latter calculations. The dotted and dot-dot-dashed lines (green) are microscopic+BUU transport calculations from Kaskulov *et al.* [57], with and without CT, respectively. The deuterium nuclear transparency is found to be independent of P_π with 81% probability. The same probability for carbon, aluminum, copper, and gold is 11.6%, 14.3%, 1.9%, and 3.6%, respectively.

E. Comparison with model calculations

We compare our results with the calculations of Larson *et al.* [9] (solid and dashed curves), Cosyn *et al.* [56] (dot-short dash and dot-long dash curves), and Kaskulov *et al.* [57] (dotted and dot-dot-dash) in Fig. 15.

Larson *et al.* compute the nuclear transparency at the exact kinematics of this experiment using a semiclassical formula based on the eikonal approximation and a parametrization of the effects of final-state interactions (FSIs) in terms of an effective interaction. This semiclassical formula involves a single integral over the path of the outgoing pion which is suited for situations in which the kinematics of the final pion are known. The nuclear density is taken as a Woods-Saxon form with radius parameter $R = 1.1A^{1/3}$ fm and diffuseness $a = 0.54$ fm. The effective interaction is based on the quantum diffusion model of Ref. [8], which predicts the interaction of the PLC to be approximately proportional to the propagation distance z for $z < l_c$. The coherence length (or formation length) is parametrized as described in Sec. II. Larson, Miller,

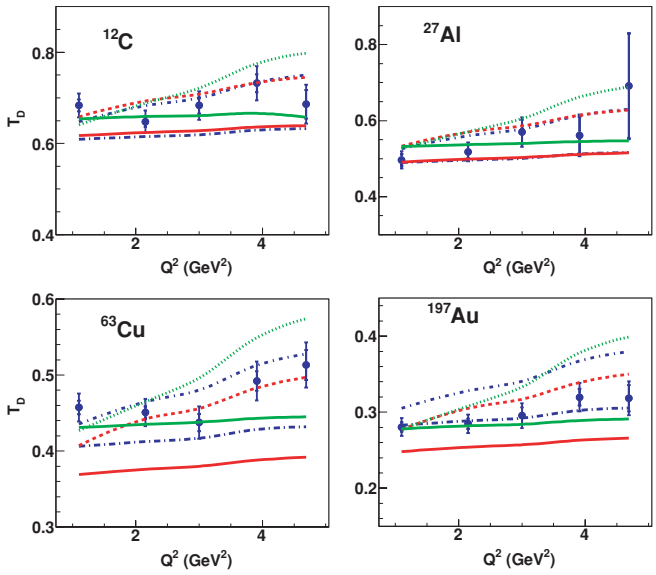

FIG. 16. (Color online) The redefined nuclear transparency T_D (see text) versus Q^2 for ^{12}C, ^{27}Al, ^{63}Cu, and ^{197}Au. The curves represent calculations identical to those in Fig. 15. The model uncertainties are identical to Fig. 15.

and Strikman use the following parameters: $T_{\text{lifetime}} = 1$ fm/c and $M_h^2 = 0.7$ (GeV/c^2)^2. In the limit of $l_c = 0$, a PLC is not created and the effective interaction reduces to a Glauber-type calculation with $\sigma_{\text{eff}} \approx \sigma_{\pi N}(P_\pi)$, the π-N cross section for pion momentum P_π obtained from a parametrization by the Particle Data Group (PDG) [58].

Cosyn *et al.* calculate the nuclear transparency as a ratio of differential cross section for pion electroproduction in a relativistic multiple-scattering Glauber approximation (RMSGA) integrated over the kinematic range of the experiment to that in a relativistic plane-wave impulse approximation (RPWIA). In the RPWIA, all particles are taken to be relativistic plane waves, while in the RMSGA, the wave function of the spectator nucleon and the outgoing pion is taken to be a convolution of a relativistic plane wave and a Glauber-type eikonal phase operator that parametrizes the effects of FSI. The parametrization chosen by these authors reflects the diffractive nature of nucleon-nucleon ($N'N$) and pion-nucleon (πN) collisions at intermediate energies. The parameters σ_{iN}^{tot} (total cross section, with i as the outgoing pion or nucleon), β_{iN} (slope parameter), and ϵ_{iN} (ratio of real to imaginary part of the scattering amplitude) were obtained by fits to the $N'N \to N'N$ databases from the PDG [58], for $i = N'$. For $i = \pi$, the parameters were obtained from fits to PDG [58] databases, SAID [59], and Ref. [60]. For outgoing nucleons with kinetic energy lower than ~300 MeV, the Glauber formalism is no longer applicable and the FSI was parametrized in a relativistic optical model eikonal approximation [61], with the global (S-V) optical model parametrization of Cooper *et al.* [62]. CT was incorporated by replacing the total cross-section parameter σ_{iN}^{tot} with an effective one based on the quantum diffusion model [8], this mirrors the effective interaction parameter of Larson *et al.*, described earlier. The parameters used for l_c were exactly the same for both sets of authors. Cosyn *et al.* also include the effects of short-range correlations (SRCs) in their calculations. The Glauber phase factor described previously is corrected for SRCs by replacing the single nucleon density typically used in Glauber-type calculations with an effective density. The effective density modifies the single nucleon density with a Jastrow correlation function and normalization functions that ensure the integral of the effective density is equal to the total number of nucleons.

Kaskulov *et al.* calculate nuclear transparency as the ratio of their model differential cross section calculated in the laboratory frame, with and without FSI, where both types of model cross sections are integrated over the kinematic range of the experiment. Their model is built around a microscopic description [48] of the elementary ^{1}H$(e,e'\pi^+)n$ process, which is divided into a soft hadronic part and a hard partonic or deep inelastic scattering production part. For the reaction on nuclei, the elementary interaction is kept the same and standard effects, such as Fermi motion, Pauli blocking, and nuclear shadowing, are accounted for. Finally, all produced prehadrons and hadrons are propagated through the nuclear medium according to the Boltzmann-Uehling-Uhlenbeck (BUU) transport equation. The DIS contribution to the cross section is determined by the Lund fragmentation model [63] and the time development of the interactions of the prehadron is determined by the quantum diffusion model [8]. The production time and the formation time are from a Monte Carlo calculation based on the Lund fragmentation model [63] described in Ref. [64]. Only the DIS part of the cross section is effected by this prehadronic interaction and thus in this model only the DIS events are responsible for the CT effect.

Our results are in good agreement with the CT calculations of Larson *et al.*, while the calculations of both Cosyn *et al.* and Kaskulov *et al.* overestimate the P_π dependence of the data. However, whereas one can argue about details of the calculation, it is more important to note that the trend of all calculations including CT in Figs. 15 and 16 are consistent with the trend of the nuclear transparency data versus Q^2.

The underlying cause for the rise in nuclear transparency is different for the different model calculations, however. While the longitudinal-photon production mechanism is expected to dominate exclusive $(e,e'\pi^+)$ production at asymptotic Q^2, leading one to anticipate CT effects entering via the longitudinal channel, the Kaskulov *et al.* calculations find the CT effects to come from the transverse-photon production mechanism. Thus, we separately show in Fig. 15 the nuclear transparency results for our low-ϵ data (but note that the calculations shown in Figs. 15 and 16 are for the high-ϵ kinematics only). Clearly, within the experimental uncertainties, we do not see any obvious difference between the nuclear transparency results measured at (high) $\epsilon = 0.56$ at $Q^2 = 2.15$ (GeV)^2 and $\epsilon = 0.39$ at $Q^2 = 3.91$ (GeV)^2 and at (low) $\epsilon = 0.27$ at $Q^2 = 2.16$ (GeV)^2 and $\epsilon = 0.25$ at $Q^2 = 4.01$ (GeV)^2. In these measurements $\Delta\epsilon = 0.29$ at $Q^2 = 2.15$ (GeV)^2 and $\Delta\epsilon = 0.14$ at $Q^2 \approx 4$ (GeV)^2. Given the uncertainties of the present experiment, we cannot distinguish between the suggested mechanisms.

F. Further studies of the CT mechanism

Figures 15 and 16 show a rise of nuclear transparency with outgoing pion momentum, or alternatively Q^2, which deviates from the traditional nuclear physics expectation. However, as can be readily seen in Table I, there exists a strong correlation between the outgoing pion momentum, P_π, and the magnitude of the virtual-pion (three-)momentum, k_π. This poses a potential pitfall in that the observed CT-like behavior could be an artifact of the increased values of k_π (and thus an increased probability for reaction mechanisms beyond the quasifree picture), rather than a dependence on P_π. To investigate this further, we performed measurements at different values of k_π (and thus different P_π), but at identical Q^2 (2.15 GeV^2).

The results are shown in Fig. 17 and indicate that the nuclear transparency does not show any obvious dependence on k_π. This result rules out the possibility that nuclear transparency *only* depends on k_π (but does not yet rule out the possibility that nuclear transparency depends on k_π, as well as other variables).

The values of Q^2 and P_π for this exclusive $(e,e'\pi^+)$ experiment are also strongly correlated. Because the size of the PLC is in general related to Q^2, and the formation length of the PLC to P_π, the rise in nuclear transparency results can also be a mixed PLC-size-and-formation-length effect. To investigate which of these two effects dominates, we formed nuclear transparency ratios of the heavy target nuclei (^{27}Al, ^{63}Cu, and ^{197}Au) with respect to ^{12}C, termed as T_C. These ratios should be less sensitive to formation length effects. Here, we use the nuclear size as a yardstick to gauge formation length effects.

The "super ratios," T_C, for ^{27}Al (top left panel), ^{63}Cu (top right panel), and ^{197}Au (bottom left panel) are shown in Fig. 18. The results are consistent with a flat line, within the (large) experimental uncertainties, with probabilities of 0.32, 0.40, and 0.64, respectively. A plausible explanation is that the pion formation length in our kinematics is already much larger than the nuclear radius (a simple estimate gives a formation length of order 10 fm). We also note that a reasonable approximation for the coherence length of the virtual photon [$l_c = 1/(2Mx)$] renders a value of about 0.2–0.5 fm, which is much smaller than the size of the nucleus. Thus, we should not be sensitive to any coherence length effects. We conclude that the observed rise in nuclear transparency is likely attributable to a small PLC size, rather than a PLC formation length effect.

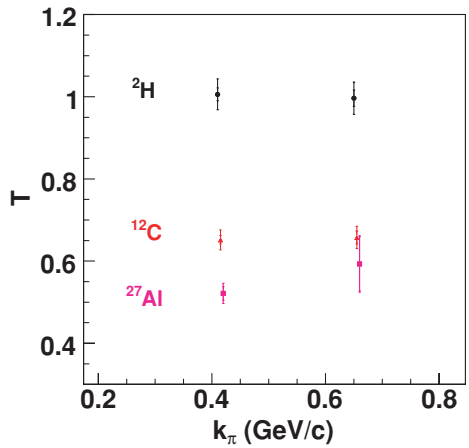

FIG. 17. (Color online) Nuclear transparency, T, vs k_π for ^{2}H, ^{12}C, and ^{27}Al.

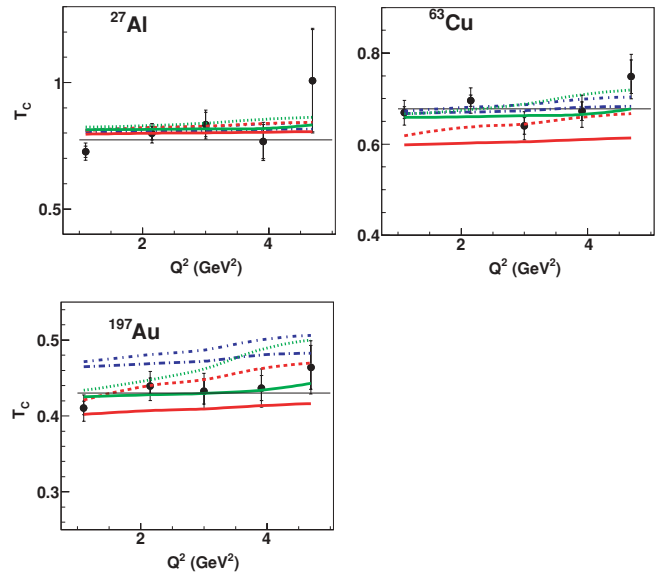

FIG. 18. (Color online) The T_C vs Q^2, where T_C is defined as the super ratio of the heavy nuclear targets with respect to ^{12}C [$T(A > 12)$ to $T(A = 12)$]. The inner error bars are the statistical uncertainties, the outer error bars are the statistical and point-to-point systematic uncertainties added in quadrature. The probabilities of a straight line fit are 32%, 40%, and 64% for carbon, copper and gold targets, respectively. The calculations are same as in Fig. 15, but divided by the results for ^{12}C.

G. The *A* dependence

The dependence of the nuclear transparency data on the nucleon number A gives further insight on the proper interpretation of the data in terms of an onset of CT. This goes beyond the Q^2 (or P_π) dependence of nuclear transparencies for one single nuclear target described previously. Here, the entire nuclear transparency data set was examined using a single parameter fit to $T = A^{\alpha-1}$, where A is the nucleon number and α is the free parameter (for each value of Q^2). Using only one parameter obviously neglects specific surface effects of the various nuclei, but it has proven to be an effective way to describe the bulk properties of the nuclear medium. For example, pion-nucleus scattering total cross section data are well described using such a single parameter fit, $\sigma^A = A^\alpha \sigma^N$, where σ^A is the nuclear cross section, σ^N is the nucleon cross section, and $\alpha = 0.76$ [65]. No noticeable dependence on the incident pion energy was measured, similar to the lack of k_π dependence seen here.

Fits to the full nuclear transparency data set with $T = A^{\alpha-1}$ for $A > 1$ are shown as the solid black curves in Fig. 19 and listed under the second column heading in Table V. The total uncertainties in α are determined by fitting the experimental data with the statistical and overall

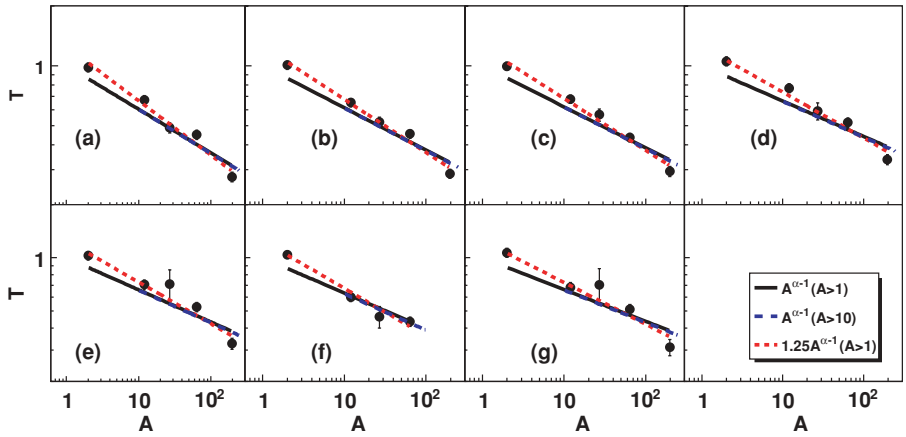

FIG. 19. (Color online) The nuclear transparency vs the nucleon number, A, for (a) $\epsilon = 0.5$, $Q^2 = 1.1$ GeV^2, (b) $\epsilon = 0.56$, $Q^2 = 2.15$ GeV^2, (c) $\epsilon = 0.45$, $Q^2 = 3.0$ GeV^2, (d) $\epsilon = 0.39$, $Q^2 = 3.9$ GeV^2, (e) $\epsilon = 0.26$, $Q^2 = 4.7$ GeV^2, (f) $\epsilon = 0.27$, $Q^2 = 2.16$ GeV^2, and, (g) $\epsilon = 0.25$, $Q^2 = 4.01$ GeV^2. The lines are fits to the experimental data using the parametrization $T = A^{\alpha-1}$ for $A > 1$ (solid black), $A > 10$ (long-dashed blue), and $T = 1.25A^{\alpha-1}$ (short-dashed red). Only the statistical uncertainties of the data are shown. The values of the parameter α is listed in Table V.

(point-to-point, normalization, and model) systematic uncertainties added in quadrature. The uncertainties in α are dominated by systematics and include fitting uncertainties and model uncertainties.

Even though the single-parameter fit $T = A^{\alpha-1}$ is simple and neglects local A-dependent shell or density effects, this does not affect the final conclusion that the A-dependence changes with Q^2. We have verified this with two methods:

(i) We find an almost identical increase of α with Q^2 when fitting *only* the data from medium-heavy nuclei, $A > 10$, as shown by the blue dashed curves in Fig. 19 and listed under the third column heading in Table V. This corroborates the results shown in Fig. 18.

(ii) The increase of α with Q^2 also remains when we change from a single-parameter fit to a two-parameter fit to $T = \beta A^{\alpha-1}$, as indicated by the red dotted curves in Fig. 19 and listed under the fourth column heading in Table V. Although the quality of the fit is better for the two-parameter form, the best fit is obtained for $\beta = 1.25$, which is unphysical for $A = 1$ because it does not satisfy the condition $T(A = 1) = 1$. Moreover, the single parameter fit describes the hadron-nucleus cross-sections for a wide range of hadrons [65], which is our motivation for comparing the electroproduction data with the same form. Thus, even though the exact value of α may come with a variety of nuclear physics uncertainties, given the simplistic form of the A dependence, we find that the empirical Q^2 dependence is well established.

In Fig. 20, we compare α as function of Q^2, extracted from the single parameter form $T = A^{\alpha-1}$, with the calculations including CT effects of Larson *et al.* [9] and Cosyn *et al.* [56]. The agreement with the calculations of Ref. [9] is excellent, but the data are systematically below the calculations (including both CT and SRC effects) of Ref. [56]. The values of α for the theoretical calculations were obtained by fitting the calculated transparency as a function of A to the form $T = A^{\alpha-1}$. As mentioned earlier, Kaskulov *et al.* [48] recently suggested that the CT effect should only exist in the transverse cross section. For this reason, we have again separately indicated the α values for the low and high ϵ values of this experiment, where applicable. Within our uncertainties, we see no indication of this prediction. However, we caution that the differences between the low- to high-ϵ kinematics in terms of contributions from the longitudinal cross sections to the total measured cross sections changes by less than 30% in our kinematics

TABLE V. α parameters extracted from three different fits. The fit quality $\chi^2/N_{\rm dof}$ (χ^2 per degree of freedom) for each fit is also listed. The first fit is to $T = A^{\alpha-1}$ for data with $A > 1$. The obtained α values along with the total uncertainties are listed. To indicate the increase in α with Q^2, we also show the ratio $\frac{\alpha(Q^2)}{\alpha(Q^2=1.1)}$ and its uncertainty. The second fit is to $A^{\alpha-1}$, but only for data with $A > 10$. The third fit is to $T = \beta A^{\alpha-1}$ for data with $A > 1$. The quality of fit was best for $\beta = 1.25$; however, it does not satisfy the condition $T = 1$ for $A = 1$. The parameter α shows a similar and consistent increase with Q^2 for all three fits. The total uncertainties for the $A > 10$ and the two parameter fit are very similar to the ones shown for the first fit and hence they are not shown.

Setting	$A^{\alpha-1}$ for A > 1					$A^{\alpha-1}$ for A > 10			$1.25A^{\alpha-1}$ for A > 1		
Q^2 (GeV/c)^2	α	Uncert.	$\chi^2/N_{\rm dof}$	$\frac{\alpha(Q^2)}{\alpha(Q^2=1.1)}$	Uncert.	α	$\chi^2/N_{\rm dof}$	$\frac{\alpha(Q^2)}{\alpha(Q^2=1.1)}$	α	$\chi^2/N_{\rm dof}$	$\frac{\alpha(Q^2)}{\alpha(Q^2=1.1)}$
1.1	0.785	0.007	5.54	1	–	0.784	5.56	1	0.731	2.05	1
2.15	0.798	0.006	6.15	1.017	0.012	0.795	5.14	1.014	0.739	1.45	1.011
2.23[a]	0.804	0.012	3.68	1.024	0.017	0.797	0.29	1.017	0.730	1.06	0.999
3.0	0.799	0.007	5.53	1.018	0.013	0.796	4.84	1.015	0.740	1.12	1.012
3.91	0.831	0.007	7.47	1.059	0.013	0.827	6.52	1.055	0.775	1.84	1.062
4.0[a]	0.831	0.010	4.09	1.059	0.016	0.827	2.59	1.055	0.769	1.11	1.052
4.69	0.826	0.009	4.61	1.052	0.015	0.822	4.04	1.048	0.770	1.61	1.053

[a]Data taken at low ϵ values.

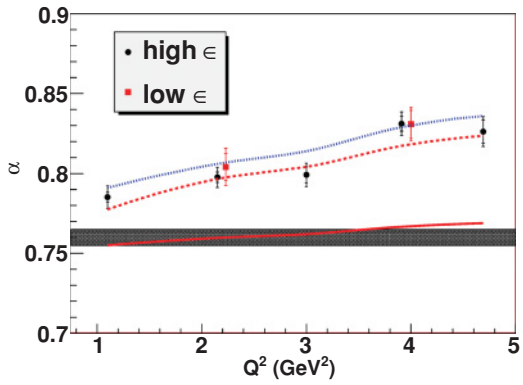

FIG. 20. (Color online) The parameter α, as extracted from the global nuclear data set of this experiment [from $T = A^{(\alpha-1)}$] versus Q^2 (solid black circles). The inner error bars indicate the statistical uncertainties, and the outer error bars are the quadrature sum of statistical, systematic and modeling uncertainties. The hatched band is the value of α extracted from pion-nucleus scattering data [65]. The solid, dashed and dotted lines are α obtained from fitting the A-dependence of the theoretical calculations: the Glauber and Glauber + CT calculations of Ref. [9], and the Glauber + CT (including SRC effects) calculations of Ref. [56], respectively. The red circles in addition show the α values extracted at low ϵ for two values of Q^2. The values of ϵ at each Q^2 point can be found in Table I and the caption of Fig. 19.

(see Fig. 12 and Table I). It is thus very well possible that the measured effect is solely attributable to the transverse contributions.

X. CONCLUSIONS

The $A(e,e'\pi^+)$ reaction was studied for a variety of nuclear targets: ^{1}H, ^{2}H, ^{12}C, ^{27}Al, Cu, and Au. Data were taken up to $Q^2 = 4.7$ GeV^2 and analyzed in terms of nuclear transparencies, the escape probability of the positively charged pion from the nuclear medium. A rise of the nuclear transparency with Q^2 (or pion momentum) could signal an onset of CT, expected to occur at large values of Q^2 from both perturbative and nonperturbative QCD.

The most convincing prior evidence for the existence of a CT effect is the analysis of Fermilab E791 data on the diffractive dissociation in two jets. However, conclusive proof of the *onset* of CT is more elusive, although hints of it were recently seen in the analysis of ρ vector meson data at fixed coherence length [22] and π^- photoproduction [26]. Our results show a far more conclusive onset of CT over the relatively large range in pion momentum between 2.5 and 4.5 GeV/c and Q^2 between 1.1 and 4.7 GeV^2. Our results are also in good agreement with model calculations including the CT effect of Larson *et al.*, Cosyn *et al.*, and Kaskulov *et al.* [9,56,57]. The latter calculation also agrees excellently with the measured $-t$ dependence of the differential cross sections, giving further credence to the onset of CT.

Specialized data sets were added to ensure that the noted rise of nuclear transparencies is indeed attributable to CT. In particular, the cross checks performed are:

(i) *L/T character of the cross section*. Within uncertainties, we find the longitudinal-transverse character of the pion electroproduction cross sections off protons and off heavier nuclei to be similar. This supports a quasifree reaction mechanism.

(ii) *Virtual-pion momentum k_π*. The measured nuclear transparencies do not appear to depend on the virtual-pion (three-)momentum, which could be a signal for increased reaction mechanism effects beyond the quasifree picture. This suggests that reaction mechanism effects beyond the quasifree reaction are suppressed.

(iii) *Cross-section ratios for medium to heavy nuclei*. "Super ratios" of the heavier target nuclei (^{27}Al, ^{63}Cu, ^{197}Au) with respect to ^{12}C show similar increases in nuclear transparency, indicating that the pion formation lengths probed in this work are already far longer than the nuclear radii.

(iv) *A dependence*. The A dependence of the data was described by a single parameter function, $T = A^{\alpha-1}$. The α values were found to be consistently larger than the 0.76 value found from pion-nucleus total cross section data, *and* rising with Q^2, consistent with a CT ansatz.

Furthermore, the results presented here are with nearly constant and small coherence lengths (0.2–0.5 fm), such that possible complications owing to π-ρ exchange terms are minimized.

These results are consistent with the predicted early onset of CT in mesons compared to baryons and, together with previous meson transparency measurements [22,26], suggest a gradual transition to meson production with small interquark separation. These results put significant constraints on early models of CT, which predict a dramatic transition with a thresholdlike behavior. The unambiguous observation of the onset of CT uniquely points to the role of color degrees of freedom in exclusive high-Q^2 processes. Furthermore, it is an effective signature of the approach to the factorization regime in meson electroproduction experiments, necessary for the access to GPDs. These results will be further extended by data to be taken after the Jefferson Lab upgrade to 12 GeV, with planned exclusive $A(e,e'\pi^+)$ measurements up to $Q^2 \approx 10$ GeV^2 [66].

ACKNOWLEDGMENTS

The authors acknowledge the outstanding support of the Jefferson Lab Hall C and Accelerator Division scientific and technical staff during this experiment. This work was supported in part by the US Department of Energy. The Southeastern Universities Research Association (SURA) operates the Thomas Jefferson National Accelerator Facility for the United States Department of Energy under Contract No. DE-AC05-84150. We acknowledge additional research grants from the US National Science Foundation and the Natural Sciences and Engineering Research Council of Canada (NSERC).

APPENDIX A

TABLE VI. Extracted cross sections and their uncertainties for hydrogen target data.

Target	Q^2 (GeV^2)	W (GeV)	$-t$ (GeV^2)	P_π (GeV/c)	ϵ	$P_\pi^{\text{c.m.}}$ (GeV/c)	$\frac{d\sigma}{dt\,dP_\pi^{\text{c.m.}}}$ (μb/GeV^3)	Stat. err. (μb/GeV^3)	Sys. err. (μb/GeV^3)
^{1}H	1.71	2.36	0.100	3.35	0.532	0.99	3.72	0.11	0.24
^{1}H	1.80	2.33	0.117	3.31	0.538	0.97	3.46	0.11	0.23
^{1}H	1.84	2.32	0.128	3.30	0.539	0.96	3.47	0.11	0.20
^{1}H	1.87	2.31	0.136	3.30	0.538	0.96	3.04	0.10	0.19
^{1}H	1.90	2.30	0.144	3.26	0.545	0.95	3.07	0.10	0.19
^{1}H	1.93	2.28	0.152	3.24	0.548	0.94	2.92	0.09	0.17
^{1}H	1.94	2.27	0.160	3.21	0.554	0.93	2.96	0.09	0.18
^{1}H	1.95	2.27	0.167	3.21	0.555	0.93	2.78	0.09	0.17
^{1}H	2.02	2.25	0.174	3.20	0.554	0.92	2.75	0.08	0.16
^{1}H	2.06	2.24	0.181	3.19	0.553	0.91	2.54	0.08	0.15
^{1}H	2.05	2.24	0.187	3.19	0.553	0.91	2.71	0.09	0.15
^{1}H	2.09	2.23	0.193	3.17	0.555	0.90	2.61	0.09	0.14
^{1}H	2.08	2.24	0.200	3.17	0.555	0.91	2.48	0.07	0.13
^{1}H	2.09	2.23	0.208	3.17	0.554	0.90	2.38	0.07	0.12
^{1}H	2.13	2.23	0.216	3.16	0.552	0.90	2.55	0.07	0.13
^{1}H	2.13	2.23	0.224	3.16	0.552	0.90	2.27	0.07	0.11
^{1}H	2.13	2.23	0.232	3.16	0.552	0.90	2.29	0.07	0.11
^{1}H	2.20	2.19	0.240	3.10	0.563	0.88	2.21	0.07	0.11
^{1}H	2.22	2.19	0.249	3.10	0.560	0.87	2.18	0.06	0.11
^{1}H	2.19	2.19	0.259	3.10	0.563	0.88	2.15	0.07	0.11
^{1}H	2.26	2.18	0.270	3.08	0.558	0.86	2.11	0.06	0.11
^{1}H	2.29	2.17	0.283	3.08	0.557	0.86	2.05	0.06	0.12
^{1}H	2.34	2.16	0.299	3.07	0.557	0.86	1.95	0.06	0.12
^{1}H	2.44	2.13	0.317	3.06	0.556	0.84	2.11	0.07	0.15
^{1}H	2.53	2.12	0.341	3.04	0.547	0.82	1.78	0.06	0.04
^{1}H	2.63	2.08	0.385	3.03	0.561	0.82	1.83	0.07	0.19
^{1}H	3.75	2.21	0.425	3.89	0.251	0.89	0.64	0.02	0.06
^{1}H	4.00	2.14	0.548	3.80	0.255	0.85	0.58	0.02	0.06
^{1}H	4.00	2.14	0.646	3.73	0.255	0.84	0.64	0.02	0.07
^{1}H	4.21	2.07	0.758	3.63	0.261	0.80	0.70	0.02	0.07
^{1}H	2.55	2.28	0.199	3.55	0.435	0.94	1.82	0.06	0.09
^{1}H	2.64	2.26	0.236	3.52	0.433	0.93	1.70	0.05	0.09
^{1}H	2.68	2.24	0.260	3.49	0.438	0.91	1.50	0.05	0.08
^{1}H	2.72	2.23	0.280	3.46	0.441	0.91	1.41	0.05	0.07
^{1}H	2.78	2.21	0.300	3.45	0.440	0.90	1.43	0.05	0.08
^{1}H	2.85	2.19	0.320	3.42	0.443	0.88	1.42	0.04	0.08
^{1}H	2.90	2.18	0.340	3.40	0.445	0.87	1.26	0.04	0.07
^{1}H	2.94	2.16	0.360	3.38	0.445	0.86	1.36	0.04	0.07
^{1}H	2.96	2.16	0.380	3.37	0.446	0.86	1.28	0.04	0.07
^{1}H	3.06	2.13	0.400	3.33	0.450	0.84	1.26	0.04	0.07
^{1}H	3.08	2.12	0.420	3.30	0.454	0.83	1.22	0.04	0.06
^{1}H	3.11	2.11	0.445	3.29	0.454	0.82	1.16	0.03	0.06
^{1}H	3.27	2.07	0.474	3.28	0.450	0.80	1.08	0.04	0.06
^{1}H	3.25	2.08	0.508	3.25	0.447	0.80	1.09	0.04	0.06
^{1}H	3.50	1.99	0.565	3.21	0.455	0.77	1.22	0.04	0.07
^{1}H	0.92	2.31	0.038	2.84	0.490	0.96	10.74	0.32	0.53
^{1}H	0.98	2.29	0.047	2.81	0.497	0.94	9.56	0.26	0.49
^{1}H	1.00	2.28	0.053	2.80	0.499	0.94	8.99	0.26	0.46

TABLE VI. (*Continued.*)

Target	Q^2 GeV^2	W GeV	$-t$ GeV^2	P_π GeV/c	ϵ	P_π^{CM} GeV/c	$\frac{d\sigma}{dtdP_\pi^{CM}}$ μb/GeV^3	stat. err. μb/GeV^3	sys. err. μb/GeV^3
^{1}H	1.04	2.27	0.058	2.79	0.501	0.93	8.15	0.22	0.42
^{1}H	1.03	2.27	0.062	2.78	0.501	0.93	7.87	0.23	0.42
^{1}H	1.10	2.26	0.066	2.79	0.497	0.92	7.90	0.22	0.42
^{1}H	1.07	2.26	0.070	2.76	0.504	0.92	7.35	0.21	0.39
^{1}H	1.10	2.25	0.074	2.77	0.502	0.92	6.73	0.19	0.35
^{1}H	1.10	2.25	0.078	2.76	0.501	0.92	7.06	0.19	0.37
^{1}H	1.12	2.24	0.082	2.75	0.503	0.91	6.71	0.19	0.34
^{1}H	1.13	2.24	0.086	2.74	0.506	0.91	6.52	0.19	0.33
^{1}H	1.16	2.23	0.090	2.74	0.504	0.91	6.34	0.17	0.32
^{1}H	1.16	2.24	0.095	2.73	0.503	0.91	6.00	0.17	0.30
^{1}H	1.19	2.22	0.100	2.71	0.510	0.89	6.58	0.19	0.33
^{1}H	1.20	2.22	0.105	2.72	0.505	0.90	6.01	0.19	0.31
^{1}H	1.21	2.22	0.110	2.71	0.505	0.89	6.50	0.20	0.33
^{1}H	1.18	2.23	0.116	2.70	0.506	0.90	6.18	0.19	0.32
^{1}H	1.16	2.24	0.123	2.71	0.501	0.90	5.51	0.18	0.30
^{1}H	1.17	2.23	0.133	2.69	0.505	0.89	6.15	0.18	0.37
^{1}H	1.21	2.22	0.154	2.67	0.502	0.88	7.21	0.20	0.59
^{1}H	2.06	2.24	0.165	3.21	0.268	0.91	2.52	0.08	0.12
^{1}H	2.16	2.21	0.209	3.17	0.269	0.90	2.01	0.07	0.10
^{1}H	2.26	2.18	0.248	3.12	0.274	0.88	1.95	0.06	0.10
^{1}H	2.27	2.18	0.290	3.07	0.276	0.86	1.97	0.06	0.10
^{1}H	2.28	2.18	0.326	3.02	0.274	0.85	2.04	0.07	0.13
^{1}H	1.81	1.86	0.241	2.21	0.634	0.68	5.74	0.19	0.43
^{1}H	1.86	1.84	0.276	2.17	0.634	0.67	5.01	0.16	0.33
^{1}H	1.93	1.82	0.305	2.15	0.633	0.65	5.10	0.15	0.31
^{1}H	2.00	1.79	0.330	2.12	0.636	0.63	5.20	0.18	0.31
^{1}H	2.08	1.76	0.355	2.09	0.638	0.62	5.59	0.15	0.32
^{1}H	2.14	1.74	0.385	2.07	0.637	0.60	5.61	0.15	0.32
^{1}H	2.19	1.74	0.414	2.07	0.629	0.60	5.73	0.16	0.33
^{1}H	2.25	1.71	0.444	2.04	0.630	0.58	5.58	0.18	0.30
^{1}H	2.30	1.70	0.479	2.02	0.628	0.57	5.61	0.19	0.30
^{1}H	2.40	1.67	0.548	1.98	0.622	0.55	5.58	0.17	0.29
^{1}H	4.39	2.32	0.469	4.49	0.259	0.96	0.45	0.02	0.02
^{1}H	4.71	2.24	0.621	4.37	0.265	0.91	0.41	0.01	0.02
^{1}H	4.82	2.21	0.765	4.28	0.269	0.90	0.41	0.01	0.02
^{1}H	4.98	2.17	0.914	4.17	0.267	0.86	0.43	0.01	0.02
^{1}H	3.45	2.38	0.280	4.24	0.381	1.00	0.75	0.02	0.04
^{1}H	3.55	2.36	0.340	4.20	0.381	0.99	0.71	0.02	0.04
^{1}H	3.69	2.32	0.380	4.17	0.383	0.97	0.67	0.02	0.04
^{1}H	3.78	2.30	0.420	4.12	0.386	0.95	0.68	0.02	0.04
^{1}H	3.84	2.28	0.460	4.09	0.386	0.93	0.62	0.02	0.03
^{1}H	3.91	2.26	0.499	4.05	0.388	0.92	0.59	0.02	0.03
^{1}H	3.92	2.25	0.540	4.00	0.393	0.91	0.62	0.02	0.03
^{1}H	4.00	2.23	0.579	3.97	0.395	0.90	0.63	0.02	0.03
^{1}H	4.10	2.21	0.619	3.93	0.395	0.88	0.61	0.02	0.03
^{1}H	4.30	2.15	0.663	3.91	0.394	0.85	0.66	0.02	0.03
^{1}H	4.40	2.12	0.741	3.87	0.398	0.84	0.63	0.02	0.03

APPENDIX B

TABLE VII. Extracted cross sections and their uncertainties for deuterium target data.

Target	Q^2 (GeV^2)	W (GeV)	$-t$ (GeV^2)	P_π (GeV/c)	$P_\pi^{\text{c.m.}}$ (GeV/c)	ϵ	$\frac{d\sigma}{dt\,d\,P_\pi^{\text{c.m.}}}$ (μb/GeV^3)	Stat. err. (μb/GeV^3)	Sys. err. (μb/GeV^3)
^{2}H	2.24	3.68	0.177	3.20	1.35	0.559	17.36	0.63	1.30
^{2}H	2.24	3.68	0.188	3.19	1.34	0.559	31.72	1.16	1.82
^{2}H	2.24	3.68	0.195	3.18	1.34	0.559	45.58	1.73	2.60
^{2}H	2.24	3.68	0.203	3.17	1.34	0.559	55.31	2.03	3.10
^{2}H	2.24	3.68	0.211	3.16	1.33	0.559	64.42	2.48	3.72
^{2}H	2.24	3.68	0.220	3.15	1.33	0.559	66.01	2.42	3.98
^{2}H	2.24	3.68	0.229	3.14	1.32	0.559	59.77	2.20	3.78
^{2}H	2.24	3.68	0.240	3.13	1.32	0.559	53.28	2.00	3.51
^{2}H	2.24	3.68	0.251	3.12	1.31	0.559	41.23	1.55	2.78
^{2}H	2.24	3.68	0.263	3.10	1.31	0.559	27.73	1.03	1.86
^{2}H	2.24	3.68	0.277	3.08	1.30	0.559	15.29	0.61	1.01
^{2}H	2.24	3.68	0.299	3.04	1.28	0.559	7.86	0.28	0.46
^{2}H	4.00	3.86	0.442	3.90	1.43	0.254	4.65	0.21	0.58
^{2}H	4.00	3.86	0.512	3.84	1.41	0.254	10.20	0.43	1.25
^{2}H	3.02	3.73	0.290	3.46	1.37	0.449	6.75	0.25	0.47
^{2}H	3.02	3.73	0.316	3.42	1.36	0.449	17.55	0.66	1.13
^{2}H	3.02	3.73	0.337	3.40	1.35	0.449	24.30	0.92	1.49
^{2}H	3.02	3.73	0.359	3.38	1.34	0.449	25.32	0.98	1.50
^{2}H	3.02	3.73	0.380	3.36	1.33	0.449	22.72	1.00	1.28
^{2}H	3.02	3.73	0.402	3.34	1.32	0.449	16.21	0.65	0.91
^{2}H	1.12	3.60	0.067	2.78	1.30	0.504	188.27	6.96	11.29
^{2}H	1.12	3.60	0.071	2.78	1.30	0.504	262.48	9.75	14.97
^{2}H	1.12	3.60	0.077	2.77	1.29	0.504	310.24	11.76	18.10
^{2}H	1.12	3.60	0.082	2.76	1.29	0.504	316.58	12.18	19.00
^{2}H	1.12	3.60	0.088	2.75	1.29	0.504	268.56	10.35	16.58
^{2}H	1.12	3.60	0.094	2.75	1.29	0.504	211.69	7.88	13.73
^{2}H	1.12	3.60	0.099	2.74	1.28	0.504	144.49	5.42	9.61
^{2}H	1.12	3.60	0.105	2.72	1.27	0.504	75.80	3.03	4.91
^{2}H	1.12	3.60	0.111	2.70	1.27	0.504	36.38	1.60	2.26
^{2}H	1.12	3.60	0.120	2.68	1.25	0.504	16.95	0.98	0.95
^{2}H	1.12	3.60	0.128	2.66	1.24	0.504	9.92	0.69	0.54
^{2}H	2.24	3.68	0.193	3.19	1.34	0.274	36.94	1.41	3.80
^{2}H	2.24	3.68	0.221	3.15	1.33	0.274	58.50	2.38	7.07
^{2}H	2.24	3.68	0.248	3.12	1.32	0.274	40.19	1.56	4.88
^{2}H	2.24	3.68	0.293	3.06	1.29	0.274	8.69	0.31	1.05
^{2}H	2.14	3.17	0.314	2.17	0.99	0.630	24.32	0.98	1.78
^{2}H	2.14	3.17	0.346	2.14	0.98	0.630	60.74	2.25	4.07
^{2}H	2.14	3.17	0.367	2.11	0.97	0.630	83.29	3.10	5.98
^{2}H	2.14	3.17	0.385	2.09	0.96	0.630	89.87	3.22	7.08
^{2}H	2.14	3.17	0.404	2.07	0.95	0.630	66.90	2.65	5.57
^{2}H	2.14	3.17	0.424	2.05	0.94	0.630	48.89	1.85	4.44
^{2}H	2.14	3.17	0.451	2.02	0.92	0.630	27.91	1.18	2.74
^{2}H	2.14	3.17	0.481	1.98	0.91	0.630	18.00	0.93	1.99
^{2}H	4.74	4.06	0.507	4.48	1.55	0.264	2.76	0.10	0.34
^{2}H	4.74	4.06	0.592	4.40	1.52	0.264	5.54	0.22	0.67
^{2}H	4.74	4.06	0.668	4.34	1.50	0.264	5.31	0.22	0.65
^{2}H	3.94	3.98	0.359	4.18	1.52	0.391	2.47	0.09	0.27
^{2}H	3.94	3.98	0.393	4.15	1.51	0.391	6.20	0.23	0.57
^{2}H	3.94	3.98	0.417	4.12	1.50	0.391	9.38	0.35	0.77
^{2}H	3.94	3.98	0.442	4.10	1.49	0.391	11.94	0.44	0.95
^{2}H	3.94	3.98	0.469	4.08	1.48	0.391	10.97	0.42	0.89
^{2}H	3.94	3.98	0.496	4.05	1.48	0.391	10.04	0.41	0.85
^{2}H	3.94	3.98	0.525	4.03	1.47	0.391	8.22	0.31	0.76

TABLE VIII. Extracted cross sections and their uncertainties for carbon target data (natural isotopic abundance).

Target	Q^2 (GeV^2)	W (GeV)	$-t$ (GeV^2)	P_π (GeV/c)	$P_\pi^{\text{c.m.}}$ (GeV/c)	ϵ	$\frac{d\sigma}{dt\,d\,P_\pi^{\text{c.m.}}}$ (μb/GeV^3)	Stat. err. (μb/GeV^3)	Sys. err. (μb/GeV^3)
$^{\text{nat}}$C	2.24	14.01	0.159	3.23	2.51	0.558	26.45	1.02	2.02
$^{\text{nat}}$C	2.24	14.01	0.177	3.21	2.49	0.558	41.07	1.61	2.94
$^{\text{nat}}$C	2.24	14.01	0.189	3.20	2.48	0.558	50.06	1.76	3.26
$^{\text{nat}}$C	2.24	14.01	0.200	3.18	2.47	0.558	54.14	2.09	3.35
$^{\text{nat}}$C	2.24	14.01	0.209	3.17	2.46	0.558	49.20	1.88	3.28
$^{\text{nat}}$C	2.24	14.01	0.218	3.16	2.45	0.558	57.30	2.12	3.51
$^{\text{nat}}$C	2.24	14.01	0.227	3.14	2.44	0.558	53.93	2.01	3.37
$^{\text{nat}}$C	2.24	14.01	0.237	3.13	2.43	0.558	56.09	2.08	3.35
$^{\text{nat}}$C	2.24	14.01	0.246	3.12	2.42	0.558	51.33	1.92	3.17
$^{\text{nat}}$C	2.24	14.01	0.257	3.10	2.41	0.558	47.62	1.77	2.95
$^{\text{nat}}$C	2.24	14.01	0.271	3.08	2.39	0.558	42.88	1.48	2.84
$^{\text{nat}}$C	4.04	14.59	0.388	3.96	2.91	0.257	4.79	0.32	0.61
$^{\text{nat}}$C	4.04	14.59	0.498	3.85	2.83	0.257	7.08	0.36	0.91
$^{\text{nat}}$C	3.02	14.22	0.261	3.49	2.65	0.450	14.12	0.55	1.77
$^{\text{nat}}$C	3.02	14.22	0.315	3.43	2.61	0.450	20.13	0.66	2.57
$^{\text{nat}}$C	3.02	14.22	0.367	3.37	2.56	0.450	22.06	0.69	2.78
$^{\text{nat}}$C	1.12	13.67	0.071	2.78	2.24	0.504	95.54	3.80	9.86
$^{\text{nat}}$C	1.12	13.67	0.079	2.77	2.23	0.504	231.96	8.73	25.10
$^{\text{nat}}$C	1.12	13.67	0.085	2.76	2.22	0.504	253.64	9.85	29.19
$^{\text{nat}}$C	1.12	13.67	0.089	2.75	2.21	0.504	264.99	9.82	31.33
$^{\text{nat}}$C	1.12	13.67	0.094	2.74	2.20	0.504	256.93	10.00	30.78
$^{\text{nat}}$C	1.12	13.67	0.099	2.73	2.19	0.504	248.65	9.55	30.26
$^{\text{nat}}$C	1.12	13.67	0.104	2.72	2.19	0.504	229.94	9.41	26.27
$^{\text{nat}}$C	1.12	13.67	0.109	2.71	2.18	0.504	184.15	8.36	20.85
$^{\text{nat}}$C	1.12	13.67	0.113	2.70	2.17	0.504	172.23	8.24	16.81
$^{\text{nat}}$C	1.12	13.67	0.119	2.68	2.16	0.504	145.60	6.24	14.24
$^{\text{nat}}$C	1.12	13.67	0.125	2.67	2.15	0.504	129.83	6.11	10.75
$^{\text{nat}}$C	1.12	13.67	0.133	2.65	2.13	0.504	99.01	4.60	7.17
$^{\text{nat}}$C	2.24	14.01	0.181	3.21	2.49	0.275	37.50	1.60	3.05
$^{\text{nat}}$C	2.24	14.01	0.219	3.16	2.45	0.275	44.01	1.85	3.75
$^{\text{nat}}$C	2.24	14.01	0.251	3.11	2.41	0.275	45.06	1.84	3.74
$^{\text{nat}}$C	2.20	13.17	0.292	2.17	1.77	0.642	27.97	1.35	3.47
$^{\text{nat}}$C	2.20	13.17	0.335	2.13	1.73	0.642	45.35	1.84	5.66
$^{\text{nat}}$C	2.20	13.17	0.363	2.09	1.71	0.642	55.11	2.75	6.97
$^{\text{nat}}$C	2.20	13.17	0.386	2.07	1.69	0.642	56.99	2.25	7.26
$^{\text{nat}}$C	4.73	15.03	0.397	4.59	3.27	0.263	2.42	0.16	0.30
$^{\text{nat}}$C	4.73	15.03	0.500	4.50	3.21	0.263	4.04	0.19	0.51
$^{\text{nat}}$C	3.94	14.77	0.320	4.23	3.08	0.391	5.49	0.22	0.35
$^{\text{nat}}$C	3.94	14.77	0.378	4.17	3.04	0.391	8.70	0.34	0.55
$^{\text{nat}}$C	3.94	14.77	0.429	4.12	3.00	0.391	10.04	0.34	0.62

TABLE IX. Extracted cross sections and their uncertainties for aluminum target data (natural isotopic abundance).

Target	Q^2 (GeV^2)	W (GeV)	$-t$ (GeV^2)	P_π (GeV/c)	$P_\pi^{\text{c.m.}}$ (GeV/c)	ϵ	$\frac{d\sigma}{dt\,d\,P_\pi^{\text{c.m.}}}$ (μb/GeV^3)	Stat. err. (μb/GeV^3)	Sys. err. (μb/GeV^3)
$^{\text{nat}}$Al	2.11	28.20	0.172	3.22	2.84	0.554	100.26	4.31	11.57
$^{\text{nat}}$Al	2.11	28.20	0.228	3.14	2.77	0.554	82.38	3.56	7.81
$^{\text{nat}}$Al	3.99	28.87	0.404	3.94	3.37	0.256	12.90	3.32	1.58
$^{\text{nat}}$Al	2.95	28.44	0.310	3.44	2.99	0.448	38.98	2.09	5.05
$^{\text{nat}}$Al	1.11	27.79	0.077	2.78	2.49	0.502	401.69	15.79	53.74
$^{\text{nat}}$Al	1.11	27.79	0.105	2.72	2.44	0.502	312.93	11.48	27.55
$^{\text{nat}}$Al	2.07	28.21	0.186	3.21	2.82	0.267	82.96	10.66	10.93
$^{\text{nat}}$Al	2.09	27.25	0.286	2.15	1.95	0.648	81.05	9.11	10.05
$^{\text{nat}}$Al	4.57	29.41	0.458	4.54	3.81	0.261	9.44	1.86	1.18
$^{\text{nat}}$Al	3.83	29.09	0.384	4.17	3.54	0.389	15.80	1.36	2.04

TABLE X. Extracted cross sections and their uncertainties for copper target data (natural isotopic abundance).

Target	Q^2 (GeV^2)	W (GeV)	$-t$ (GeV^2)	P_π (GeV/c)	$P_\pi^{\text{c.m.}}$ (GeV/c)	ϵ	$\frac{d\sigma}{dt\,d\,P_\pi^{\text{c.m.}}}$ (μb/GeV^3)	Stat. err. (μb/GeV^3)	Sys. err. (μb/GeV^3)
$^{\text{nat}}$Cu	2.24	62.36	0.161	3.23	3.05	0.558	81.49	3.06	6.15
$^{\text{nat}}$Cu	2.24	62.36	0.183	3.21	3.03	0.558	112.51	4.20	8.81
$^{\text{nat}}$Cu	2.24	62.36	0.197	3.19	3.01	0.558	118.28	4.48	9.30
$^{\text{nat}}$Cu	2.24	62.36	0.208	3.17	2.99	0.558	131.91	5.07	9.97
$^{\text{nat}}$Cu	2.24	62.36	0.219	3.16	2.98	0.558	131.81	4.85	9.93
$^{\text{nat}}$Cu	2.24	62.36	0.230	3.14	2.96	0.558	134.78	4.92	9.81
$^{\text{nat}}$Cu	2.24	62.36	0.241	3.12	2.95	0.558	125.55	4.81	9.23
$^{\text{nat}}$Cu	2.24	62.36	0.253	3.11	2.93	0.558	122.13	4.47	8.79
$^{\text{nat}}$Cu	2.24	62.36	0.265	3.09	2.91	0.558	112.68	4.25	8.12
$^{\text{nat}}$Cu	2.24	62.36	0.278	3.07	2.90	0.558	106.16	4.28	7.61
$^{\text{nat}}$Cu	4.04	63.12	0.364	3.98	3.71	0.257	10.98	0.86	1.51
$^{\text{nat}}$Cu	4.04	63.12	0.465	3.89	3.62	0.257	17.60	0.81	2.37
$^{\text{nat}}$Cu	3.02	62.64	0.250	3.51	3.29	0.450	32.07	1.37	3.98
$^{\text{nat}}$Cu	3.02	62.64	0.305	3.45	3.24	0.450	46.62	1.40	5.01
$^{\text{nat}}$Cu	3.02	62.64	0.363	3.38	3.17	0.450	47.83	1.61	4.74
$^{\text{nat}}$Cu	1.12	61.93	0.070	2.79	2.66	0.503	122.69	4.62	9.51
$^{\text{nat}}$Cu	1.12	61.93	0.083	2.76	2.63	0.503	618.86	18.04	49.79
$^{\text{nat}}$Cu	1.12	61.93	0.091	2.75	2.62	0.503	614.14	19.83	48.08
$^{\text{nat}}$Cu	1.12	61.93	0.098	2.73	2.60	0.503	552.29	18.40	43.14
$^{\text{nat}}$Cu	1.12	61.93	0.105	2.71	2.58	0.503	542.30	16.21	39.69
$^{\text{nat}}$Cu	1.12	61.93	0.115	2.69	2.56	0.503	484.09	14.21	33.64
$^{\text{nat}}$Cu	1.12	61.93	0.126	2.67	2.54	0.503	380.04	12.93	25.42
$^{\text{nat}}$Cu	2.24	62.35	0.186	3.19	3.01	0.282	109.18	4.45	9.03
$^{\text{nat}}$Cu	2.24	62.35	0.241	3.11	2.94	0.282	109.87	4.09	8.17
$^{\text{nat}}$Cu	4.73	63.70	0.468	4.53	4.18	0.264	10.76	0.38	1.40
$^{\text{nat}}$Cu	4.73	63.70	0.647	4.36	4.02	0.264	10.77	0.64	1.42
$^{\text{nat}}$Cu	3.94	63.34	0.314	4.24	3.93	0.391	14.16	0.62	1.77
$^{\text{nat}}$Cu	3.94	63.34	0.385	4.17	3.87	0.391	21.61	0.74	2.00
$^{\text{nat}}$Cu	3.94	63.34	0.450	4.10	3.80	0.391	23.31	0.75	1.94

TABLE XI. Extracted cross sections and their uncertainties for gold target data (natural isotopic abundance).

Target	Q^2 (GeV^2)	W (GeV)	$-t$ (GeV^2)	P_π (GeV/c)	$P_\pi^{\text{c.m.}}$ (GeV/c)	ϵ	$\frac{d\sigma}{dt\,d\,P_\pi^{\text{c.m.}}}$ (μb/GeV^3)	Stat. err. (μb/GeV^3)	Sys. err. (μb/GeV^3)
$^{\text{nat}}$Au	2.16	186.68	0.164	3.23	3.17	0.557	201.07	7.93	24.37
$^{\text{nat}}$Au	2.16	186.68	0.221	3.15	3.09	0.557	247.23	6.02	29.46
$^{\text{nat}}$Au	4.03	187.48	0.438	3.92	3.82	0.256	33.28	3.04	3.15
$^{\text{nat}}$Au	3.02	186.97	0.254	3.50	3.43	0.449	63.50	3.79	9.00
$^{\text{nat}}$Au	3.02	186.97	0.323	3.43	3.36	0.449	90.51	3.56	12.80
$^{\text{nat}}$Au	1.12	186.22	0.070	2.79	2.74	0.504	149.26	6.50	14.36
$^{\text{nat}}$Au	1.12	186.22	0.083	2.76	2.72	0.504	1052.70	37.33	104.4
$^{\text{nat}}$Au	1.12	186.22	0.092	2.74	2.70	0.504	1085.12	37.20	109.3
$^{\text{nat}}$Au	1.12	186.22	0.101	2.72	2.68	0.504	1033.13	36.08	103.5
$^{\text{nat}}$Au	1.12	186.22	0.110	2.70	2.66	0.504	908.06	34.59	85.81
$^{\text{nat}}$Au	1.12	186.22	0.118	2.68	2.64	0.504	881.15	34.71	75.30
$^{\text{nat}}$Au	4.73	188.08	0.545	4.46	4.34	0.263	20.08	0.97	2.79
$^{\text{nat}}$Au	3.95	187.70	0.340	4.21	4.11	0.391	30.82	1.38	4.31
$^{\text{nat}}$Au	3.95	187.70	0.424	4.13	4.03	0.391	42.07	1.77	5.68

APPENDIX C

TABLE XII. Extracted nuclear transparencies and their uncertainties. Here, T, $T_{A,2}$, and $T_{A,12}$ are the nuclear transparencies formed with hydrogen, deuterium and carbon targets, respectively (see text for further explanation). The Q^2 dependent model uncertainties are 7.6%, 5.7%, 3.5%, 3.8%, and 3.8% for $Q^2 = 1.1$, 2.1, 3.0, 3.9, 4.7 GeV^2, respectively.

Target	Q^2 (GeV^2)	P_π (GeV/c)	k_π (GeV/c)	ϵ	T	Stat.	Sys.	$T_{A,2}$	Stat.	Sys.	$T_{A,12}$	Stat.	Sys.
^{2}H	1.1	2.8	0.23	0.50	0.98	0.02	0.03	–	–	–	–	–	–
^{2}H	2.2	3.2	0.41	0.56	1.01	0.02	0.03	–	–	–	–	–	–
^{2}H	3.0	3.4	0.56	0.45	0.99	0.02	0.04	–	–	–	–	–	–
^{2}H	3.9	4.1	0.70	0.39	1.05	0.02	0.04	–	–	–	–	–	–
^{2}H	4.7	4.4	0.79	0.26	1.03	0.03	0.04	–	–	–	–	–	–
^{2}H	2.2	3.2	0.42	0.27	1.04	0.03	0.03	–	–	–	–	–	–
^{2}H	4.0	3.9	0.71	0.25	1.07	0.04	0.04	–	–	–	–	–	–
^{2}H	2.2	2.1	0.65	0.63	1.00	0.02	0.03	–	–	–	–	–	–
^{nat}C	1.1	2.8	0.23	0.50	0.67	0.01	0.02	0.68	0.01	0.02	–	–	–
^{nat}C	2.2	3.2	0.41	0.56	0.65	0.01	0.02	0.65	0.01	0.02	–	–	–
^{nat}C	3.0	3.4	0.56	0.45	0.68	0.02	0.03	0.68	0.02	0.03	–	–	–
^{nat}C	3.9	4.1	0.70	0.39	0.77	0.02	0.03	0.73	0.02	0.03	–	–	–
^{nat}C	4.7	4.4	0.79	0.26	0.70	0.03	0.03	0.69	0.03	0.03	–	–	–
^{nat}C	2.2	3.2	0.42	0.27	0.60	0.02	0.02	0.57	0.02	0.02	–	–	–
^{nat}C	4.0	3.9	0.71	0.25	0.68	0.03	0.03	0.64	0.03	0.03	–	–	–
^{nat}C	2.2	2.1	0.65	0.63	0.66	0.02	0.02	0.66	0.02	0.02	–	–	–
^{nat}Al	1.1	2.8	0.23	0.50	0.49	0.01	0.02	0.50	0.02	0.02	0.73	0.02	0.03
^{nat}Al	2.2	3.2	0.41	0.56	0.52	0.02	0.02	0.52	0.02	0.02	0.80	0.03	0.03
^{nat}Al	3.0	3.4	0.56	0.45	0.57	0.03	0.02	0.57	0.03	0.02	0.83	0.05	0.03
^{nat}Al	3.9	4.1	0.70	0.39	0.59	0.05	0.03	0.56	0.05	0.03	0.77	0.07	0.03
^{nat}Al	4.7	4.4	0.79	0.26	0.71	0.14	0.03	0.69	0.14	0.03	1.01	0.20	0.04
^{nat}Al	2.2	3.2	0.42	0.27	0.46	0.06	0.02	0.45	0.06	0.02	0.78	0.10	0.03
^{nat}Al	4.0	3.9	0.71	0.25	0.70	0.16	0.03	0.66	0.15	0.02	1.03	0.24	0.03
^{nat}Al	2.2	2.1	0.65	0.63	0.59	0.07	0.02	0.60	0.07	0.02	0.90	0.10	0.03
^{nat}Cu	1.1	2.8	0.23	0.50	0.45	0.01	0.01	0.46	0.01	0.02	0.67	0.01	0.02
^{nat}Cu	2.2	3.2	0.41	0.56	0.45	0.01	0.02	0.45	0.01	0.02	0.70	0.01	0.03
^{nat}Cu	3.0	3.4	0.56	0.45	0.43	0.01	0.02	0.44	0.01	0.02	0.64	0.02	0.03
^{nat}Cu	3.9	4.1	0.70	0.39	0.52	0.01	0.02	0.49	0.01	0.02	0.67	0.02	0.03
^{nat}Cu	4.7	4.4	0.79	0.26	0.53	0.02	0.02	0.51	0.02	0.02	0.75	0.04	0.03
^{nat}Cu	2.2	3.2	0.42	0.27	0.43	0.02	0.02	0.42	0.01	0.02	0.73	0.03	0.03
^{nat}Cu	4.0	3.9	0.71	0.25	0.51	0.02	0.02	0.48	0.02	0.02	0.75	0.04	0.03
^{nat}Au	1.1	2.8	0.23	0.50	0.28	0.01	0.01	0.28	0.01	0.01	0.41	0.01	0.02
^{nat}Au	2.2	3.2	0.41	0.56	0.29	0.01	0.01	0.28	0.01	0.01	0.44	0.01	0.02
^{nat}Au	3.0	3.4	0.56	0.45	0.29	0.01	0.01	0.30	0.01	0.01	0.43	0.02	0.02
^{nat}Au	3.9	4.1	0.70	0.39	0.34	0.01	0.02	0.32	0.01	0.01	0.44	0.02	0.02
^{nat}Au	4.7	4.4	0.79	0.26	0.33	0.02	0.02	0.32	0.02	0.01	0.46	0.03	0.02
^{nat}Au	4.0	3.9	0.71	0.25	0.31	0.03	0.02	0.29	0.03	0.01	0.46	0.05	0.02

[1] A. H. Mueller, in *Proceedings of the Seventeenth Recontre de Moriond Conference on Elementary Particle Physics, Les Arcs, France, 1982* edited by J. Tran Thanh Van (Editions Fronriers, Gif-sur-Yvette, France, 1982); S. J. Brodsky, in *Proceedings of the Thirteenth International Symposium on Multiparticle Dynamics, Volendam, The Netherlands, 1982*, edited by W. Kittel *et al.* (World Scientific, Singapore, 1983).

[2] S. J. Brodsky and A. H. Mueller, Phys. Lett. B **206**, 685 (1988).

[3] B. Blattel, G. Baym, L. L. Frankfurt, and M. Strikman, Phys. Rev. Lett. **70**, 896 (1993).

[4] J. C. Collins, L. Frankfurt, and M. Strikman, Phys. Rev. D **56**, 2982 (1997).

[5] X. Ji, Phys. Rev. Lett. **78**, 610 (1997); Phys. Rev. D **55**, 7114 (1997); A. V. Radyushkin, Phys. Lett. B **380**, 417 (1996); Phys. Rev. D **56**, 5524 (1997).

[6] M. Strikman, Nucl. Phys. A **663-664**, 64c (2000).

[7] B. Clasie *et al.*, Phys. Rev. Lett. **99**, 242502 (2007).

[8] G. R. Farrar, H. Liu, L. L. Frankfurt, and M. I. Strikman, Phys. Rev. Lett. **61**, 686 (1988).

[9] A. Larson, G. A. Miller, and M. Strikman, Phys. Rev. C **74**, 018201 (2006), arXiv:nucl-th/0604022.

[10] A. S. Carroll *et al.*, Phys. Rev. Lett. **61**, 1698 (1988).

[11] I. Mardor *et al.*, Phys. Rev. Lett. **81**, 5085 (1998).

[12] A. Leksanov *et al.*, Phys. Rev. Lett. **87**, 212301 (2001).

[13] J. P. Ralston and B. Pire, Phys. Rev. Lett. **65**, 2243 (1990).

[14] J. P. Ralston and B. Pire, Phys. Rev. Lett. **61**, 1823 (1988).

[15] S. J. Brodsky and G. F. de Teramond, Phys. Rev. Lett. **60**, 1924 (1988).

[16] N. Makins *et al.*, Phys. Rev. Lett. **72**, 1986 (1994).

[17] T. O'Neill *et al.*, Phys. Lett. B **351**, 87 (1995).

[18] K. Garrow *et al.*, Phys. Rev. C **66**, 044613 (2002).

[19] D. Abbott *et al.*, Phys. Rev. Lett. **80**, 5072 (1998).

[20] J. M. Laget, Phys. Rev. C **73**, 044003 (2006).

[21] M. R. Adams *et al.* (E665), Phys. Rev. Lett. **74**, 1525 (1995).

[22] A. Airapetian *et al.* (HERMES Collaboration), Phys. Rev. Lett. **90**, 052501 (2003).

[23] R. J. Glauber, *Lectures in Theoretical Physics*, edited by W. E. Brittin (Interscience, New York, 1959), Vol. I, p. 315.

[24] K. Ackerstaff *et al.* (HERMES Collaboration), Phys. Rev. Lett. **82**, 3025 (1999).

[25] E. M. Aitala *et al.* (E791 Collaboration), Phys. Rev. Lett. **86**, 4773 (2001).

[26] D. Dutta *et al.* (Jefferson Lab E94-104), Phys. Rev. C **68**, 021001(R) (2003).

[27] S. Nozawa and T. S. H. Lee, Nucl. Phys. A **513**, 511 (1990).

[28] A. S. Raskin and T. W. Donnelly, Ann. Phys. **191**, 78 (1989); M. Diehl and S. Sapeta, Eur. Phys. J. C **41**, 515 (2005).

[29] C. W. Leemann, D. R. Douglas, and G. A. Krafft, Annu. Rev. Nucl. Part. Sci. **51**, 413 (2001).

[30] J. R. Arrington, *Inclusive Electron Scattering From Nuclei at $x > 1$ and High Q^2*, Ph.D. thesis, California Institute of Technology, 1998.

[31] D. Dutta *et al.*, Phys. Rev. C **68**, 064603 (2003).

[32] R. Asaturyan *et al.*, Nucl. Instrum. Methods Phys. Res. A **548**, 364 (2005).

[33] T. Horn, Ph.D. thesis, University of Maryland, 2006.

[34] H. P. Blok *et al.*, Phys. Rev. C **78**, 045202 (2008); G. M. Huber *et al.*, *ibid.* **78**, 045203 (2008).

[35] D. van Westrum, Ph.D. thesis, University of Colorado, 1998.

[36] H P. Blok, T. Horn, G. Huber *et al.*, Phys. Rev. C **78**, 045202 (2008).

[37] K. Makino and M. Berz, Nucl. Instrum. Methods A **427**, 338 (1999) [http://bt.pa.msu.edu/index_cosy.htm].

[38] E. Quint, *The Proton Spectral Function of ^{27}Al*, Technical Report, NIKHEF internal note (1983).

[39] N. Makins, *Measurement of the Nuclear Dependence and Momentum Transfer Dependence of Quasi-elastic (e, e′p) Scattering at Large Momentum Transfer*, Ph.D. thesis, Massachusetts Institute of Technology, 1994.

[40] D. Gaskell, Ph.D. thesis, Oregon State University, 2001.

[41] L. W. Mo and Y. S. Tsai, Rev. Mod. Phys. **41**, 205 (1969).

[42] R. Ent, B. W. Filippone, N. C. R. Makins, R. G. Milner, T. G. O'Neill, and D. A. Wasson, Phys. Rev. C **64**, 054610 (2001).

[43] S. Fantoni and V. R. Pandharipande, Nucl. Phys. A **427**, 473 (1984).

[44] A. Aste, C. von Arx, and D. Trautmann, Z. Phys. A **26**, 167 (2005).

[45] M. E. Christy *et al.*, Phys. Rev. C **70**, 015206 (2004).

[46] V. Tvaskis, Ph.D. thesis, Vrije Universiteit te Amsterdam, 2004.

[47] M. Vanderhaeghen, M. Guidal, and J. M. Laget, Phys. Rev. C **57**, 1454 (1998); Nucl. Phys. A **627**, 645 (1997).

[48] M. M. Kaskulov, K. Gallmeister, and U. Mosel, Phys. Rev. D **78**, 114022 (2008), arXiv:0804.1834 [hep-ph].

[49] T. Horn *et al.*, Phys. Rev. C **78**, 058201 (2008).

[50] M. Battaglieri *et al.*, Phys. Rev. Lett. **87**, 172002 (2001).

[51] B. L. Friman, V. R. Pandharipande, and R. B. Wiringa, Phys. Rev. Lett. **51**, 763 (1983).

[52] D. Gaskell *et al.*, Phys. Rev. Lett **87**, 202301 (2001).

[53] J. Gomez *et al.*, Phys. Rev. D **49**, 4348 (1994).

[54] B. Frois and C. N. Papanicolas, Annu. Rev. Nucl. Part. Sci. **37**, 133 (1987).

[55] L. Lapikas, Nucl. Phys. A **553**, 297c (1993).

[56] W. Cosyn, M. C. Martinez, J. Ryckebusch, and B. Van Overmeire, Phys. Rev. C **74**, 062201(R) (2006); W. Cosyn and J. Ryckebusch (private communication).

[57] M. M. Kaskulov, K. Gallmeister, and U. Mosel, Phys. Rev. C **79**, 015207 (2009).

[58] S. Eidelman *et al.* (Particle Data Group), Phys. Lett. B **591**, 1 (2004).

[59] R. A. Arndt, W. J. Briscoe, I. I. Strakovsky, R. L. Workman, and M. M. Pavan, Phys. Rev. C **69**, 035213 (2004).

[60] T. Lasinski, R. Levi Setti, B. Schwarzschild, and P. Ukleja, Nucl. Phys. B **37**, 1 (1972).

[61] B. Van Overmeire, W. Cosyn, P. Lava, and J. Ryckebusch, Phys. Rev. C **73**, 064603 (2006).

[62] E. D. Cooper, S. Hama, B. C. Clark, and R. L. Mercer, Phys. Rev. C **47**, 297 (1993).

[63] B. Anderson *et al.*, Phys. Rep. **97**, 31 (1983).

[64] K. Gallmeister and T. Falter, Phys. Lett. B **630**, 40 (2005).

[65] A. S. Carroll *et al.*, Phys. Lett. B **80**, 319 (1979).

[66] Jefferson Lab Proposal PR12-06-107, Spokespersons: D. Dutta and R. Ent (2006).